National Technical University of Athens

School of Naval Architecture and Marine Engineering

Shipbuilding Technology Laboratory

Detection of crack growth through strain sensing in marine structures

by

Pavlos Makris

A thesis submitted in partial fulfillment of the requirements of the degree of

Master of Science in Naval Architecture and Marine Engineering

under supervision of

Konstantinos N. Anyfantis, Asst. Professor

Athens, July 2023

ΠΕΡΙΛΗΨΗ

Τα πλοία και οι θαλάσσιες κατασκευές γενικότερα εμφανίζουν ρωγμές αρκετά νωρίς στον κύκλο ζωής τους. Αν και αυτές οι ρωγμές δεν αποτελούν άμεση απειλή για την δομική ακεραιότητα της κατασκευής, όταν αλληλοεπιδρούν με το θαλάσσιο περιβάλλον κατά την λειτουργία του πλοίου, μπορούν να διαδοθούν θέτοντας σε κίνδυνο τη δομική ακεραιότητά τους. Ο τρόπος με τον οποίο αντιμετωπίζονται οι ρωγμές από την ναυτιλία είναι βασισμένος στην πρόληψη της αστοχίας. Η παρούσα διπλωματική, επικεντρώνεται σε ρωγμές λόγω κόπωσης, και στοχεύει να αναπτύξει εργαλεία που θα υποστηρίξουν ένα σύστημα παρακολούθησης της δομικής ακεραιότητας ρηγματωμένων κατασκευαστικών στοιχείων το οποίο πλέον θα στοχεύει στην πρόβλεψη της αστοχίας.

Επιγραμματικά, το πρώτο εργαλείο που αναπτύχθηκε είναι μια καινοτόμα τεχνική μελέτης της κόπωσης, η οποία αποτελεί και το κύριο μέρος αυτής της διπλωματικής. Συγκεκριμένα, η τεχνική αυτή συνδιάζει την φασματική ανάλυση με στοχαστικά μοντέλα διάδωσης ρωγμών, μέσα από ένα διακριτοποιημένο στο χρόνο μοντέλο. Λαμβάνει υπόψην τόσο την αβεβαιότητα του υλικού όσο και αυτην που οφείλεται στην κοπωτική φόρτιση η οποία προέρχεται κυρίως από θαλάσσιους κυματισμούς, στοχαστικούς εκ φύσεως. Λόγω αυτών των αβεβαιοτήτων η μέθοδος αντιμετωπίζει ορισμένες από τις παραμέτρους του φυσικού προβλήματος ως τυχαίες μεταβλητές. Για διάφορες πραγματοποιήσεις αυτών, προκύπτει εν τέλι, ένα σύνολο από διαφορετικά σενάρια για την διάδοση της ρωγμής. Περαιτέρω στατιστική ανάλυση αυτών οδηγεί σε πιθανοθεωριτικές εκτιμήσεις για τον κύκλο ζωής της κατασκευής.

Το δεύτερο εργαλείο επικεντρώνεται στην δημιουργία μας μεθοδολογίας κατασκευής υποκατάστατων μοντέλων για κατασκευαστικά στοιχεία με ρωγμές χρησιμοποιώντας την μέθοδο των πεπερασμένων στοιχείων. Τα μοντέλα αυτά υποστηρίζουν την διαδικασία επιλογής αρχιτεκτονικής για την τοποθέτηση αισθητηρων στα πλαίσια ενός συστήματος παρακολούθησης δομικής ακεραιότητας ρηγματωμένων κατασκευαστικών στοιχείων.

ABSTRACT

Cracks in ship and marine structures develop as early as the construction phase. Typically, these cracks may not immediately compromise the structural integrity of the vessel, but they have the potential to propagate when exposed to the marine environment. Presently, crack assessment primarily relies on the principles of preventive maintenance. However, this thesis is specifically dedicated to investigating fatigue cracks and aims to develop advanced tools that facilitate crack Structural Health Monitoring (SHM), enabling a shift towards predictive maintenance strategies.

The first tool developed in this research is an innovative fatigue assessment methodology, which is the principal focus of this thesis. This tool combines spectral analysis and stochastic crack growth models by incorporating a state model, two methods not often combined in the industry. The proposed framework effectively models both the material uncertainties and the randomness in the experienced ocean waves encountered by the ship which is the main contributing factor to fatigue. In order to model all these uncertainties, the proposed method treats several physical parameters as random variables. Each realization of these variables, allows for the construction of a potential crack growth path. The obtained set of stochastic crack paths is further used in order to perform reliability estimations in the entire life cycle.

The second tool aims to establish a methodology for formulating a surrogate model for a cracked structural element by employing the finite element method (FEM). The latter gives an accurate representation of the cracked structure, enabling effective and efficient sensor placement strategies, used within crack SHM systems.

ACKNOWLEDGMENTS

I am deeply grateful to my supervisor, Konstantinos Anyfantis, for his exceptional guidance and dedication during the completion of this thesis. His organizational skills have contributed to a smooth research process. I admire him for his passion for the object and his teaching methods, which have greatly expanded my knowledge and way of thinking. In addition to my supervisor, I owe a debt of gratitude to Ph.D. candidate, Nicholas Silionis, who shares the same passion and was consistently digging in the technical details with me. I am grateful I had the chance to be a part of the Ship-Hull Structural Health Monitoring (S-H SHM) group, which I consider a significant step in my career. I express my sincerest gratitude to all of its members for their passion and academic excellence.

I would also like to thank my thesis committee, which consisted of Professor Ioannis T. Georgiou, and Assistant Professor Anna D. Zervaki, for all of their helpful comments and recommendations.

I humbly extend my gratitude to my esteemed senior colleagues from the shipping industry, namely Ioannis Konidas, Tasos Sotiriou, Platonas Velonias and Dimitrios Plataras for selflessly sharing their valuable practical knowledge with me, without expecting anything in return.

Furthermore, I owe my heartfelt thanks to my esteemed colleagues from the NTUA, including Aggelos Nikomanis and Andreas Alexandris, for the invaluable exchange of ideas, knowledge, and experiences we have shared thus far. On a more personal level, I would like to express my deepest appreciation to my family for their unwavering support and encouragement. Their constant presence has been instrumental in my achievements and success.

...this thesis is dedicated to the memory of an

exceptional colleague, my beloved grandfather,

who was the catalyst for my chosen field of study.

CONTENTS

LIST OF FIGURES

7

LIST OF TABLES

1. Introduction

1.1.   Current practices

Steel ship structures are prone to developing cracks as early as during the construction stage itself and not all of them can be detected and assessed [1], [2]. Normally these cracks may not pose a direct threat to the ship structural integrity but when subjected to the marine environment are likely to propagate. Figure 1 provides an overview of the age distribution of vessels that have reported fractures [3]. This data is based on reports from the ABS in-house database, spanning the period between 2002 and 2008. It is worth noting that these vessels were not designed under the Common Structural Rules (CSR), which specifically address fatigue, a major contributing factor of flaws propagating into cracks. However, this research serves as an indicative study in understanding the prevalence of cracks in ship structures.
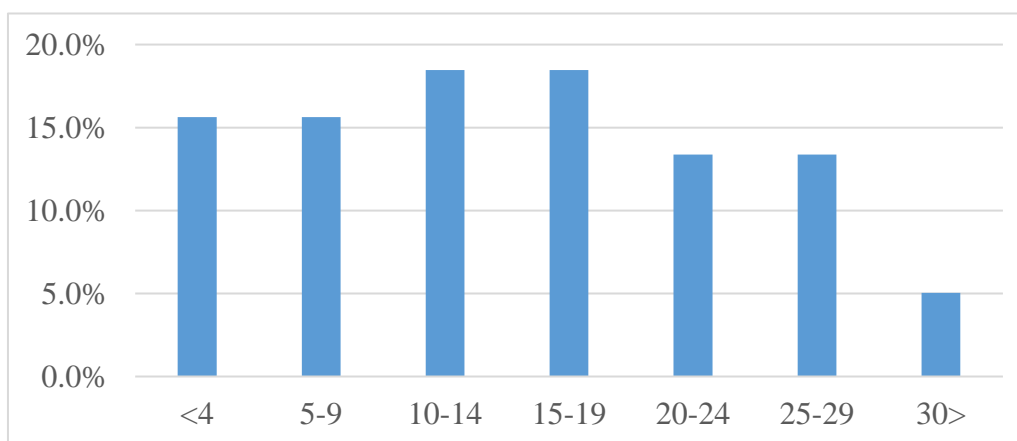
Figure 1: Vessel age when fractures were reported (data driven from [3])

In most cases fractures are found at locations of stress concentrations (50%), weld defects (40%) and metallurgical flaws (10%) [4]. Although, this is a rule of thumb, the initiation and propagation of the crack is a physical problem that inherently contains significant uncertainty. More specifically, every metallic material has imperfections and flaws in its microstructure, such as (micro)cracks, voids and inclusions initiated as soon as the machining processes [1]. Inconsistent geometries add stress concentrations and the welding contributes with weld defects in the heat affected zone [5]. All these flaws are characterized by significant uncertainty in terms of their type, direction and location, and are thus impossible to closely detect in a large scale, such as in a ship structure. Consequently, due to their role as the primary sites for crack initiation and their contribution to the rapid propagation of cracks, the inherent uncertainty associated with these flaws permeates throughout the entire process of crack initiation and propagation.

Fatigue cracking is a type of failure that develops in a material subjected to cyclic loading over a period of time, resulting in fracture at stress levels below the material's ultimate strength. Fatigue loading in marine structures mainly originates from ocean waves encountered by the ship, which are stochastic in nature. The loading combined with the microstructure of a welded material, constitute the main mechanism of fatigue crack propagation. Due to the inherent uncertainty associated with both the loading conditions and the material's microstructure, the process of fatigue crack initiation and propagation is characterized by a high degree of uncertainty.

Historically, fatigue cracks may pose a significant threat to the structural integrity, watertightness, and oil-tightness of a vessel. In adverse weather conditions, these fractures can extend to the loss of sections of the shell plating and subsequent flooding of side tanks. To mitigate these risks, in 2006 the International Association of Classification Societies (IACS) adopted the Common Structural Rules (CSR) [6] which took under consideration fatigue in ship design. After the construction of the vessel, classification societies conduct thorough hull inspections, with particular attention given to crack detection, during special/renewal surveys, typically conducted every five years. In cases where previous surveys indicate a higher likelihood of cracks, inspections may also be performed annually or during intermediate surveys.

Every stakeholder in the shipping industry, such as port state control authorities, classification societies, organizations and shipowners have a different perspective and thus, a slightly different methodology on dealing with cracks - and flaws in general - that are either detected during a hull survey or reported by seamen during operation. The USCG Critical Areas Inspection Plans (CAIP) presents a scheme for classifying structural failures to guide reporting and corrective actions [3]. The following classing process is distinguished from CAIP, as also presented in Figure 2.

- "High" criticality class or Class 1 Structural Failure. This class is assigned when during normal operating conditions exists either (1) a visible, through thickness fracture of any length in the oil-tight envelope of the outer shell where threat of pollution is a factor or, (2) a fracture or buckling which has weakened a main strength member to the extent that the safety of the vessel to operate within its design parameters is compromised [3]. In such a case, immediate corrective action must be initiated by the operator with approval of the coast guard. Temporary repairs may be permitted to allow the vessel to safely transit to a repair facility.

- "Medium" criticality class or Class 2 Structural Failure: This class is assigned to a fracture or buckling within a main strength member which does not compromise the safety of the

vessel to operate within its design parameters and does not create a threat of pollution either by location or containment [3]. In such case the necessity for corrective action shall be evaluated and agreed upon between the vessel operator and coast guard when the failure is found. Temporary repairs until the next scheduled repair period may be authorized.

- "Low" criticality class or Class 3 Structural Failure: This class is assigned to any fracture or buckling which does not otherwise meet the definition of a Class 1 or 2 structural failure or a fracture which might normally be considered a Class 2 but is determined not to be detrimental to the strength or serviceability of the effected main hull structural member [3]. In such cases corrective action or notification to the coast guard is not required. Shall be noted for the record, monitored by the operator if deemed desirable and addressed at the next regularly scheduled repair period.
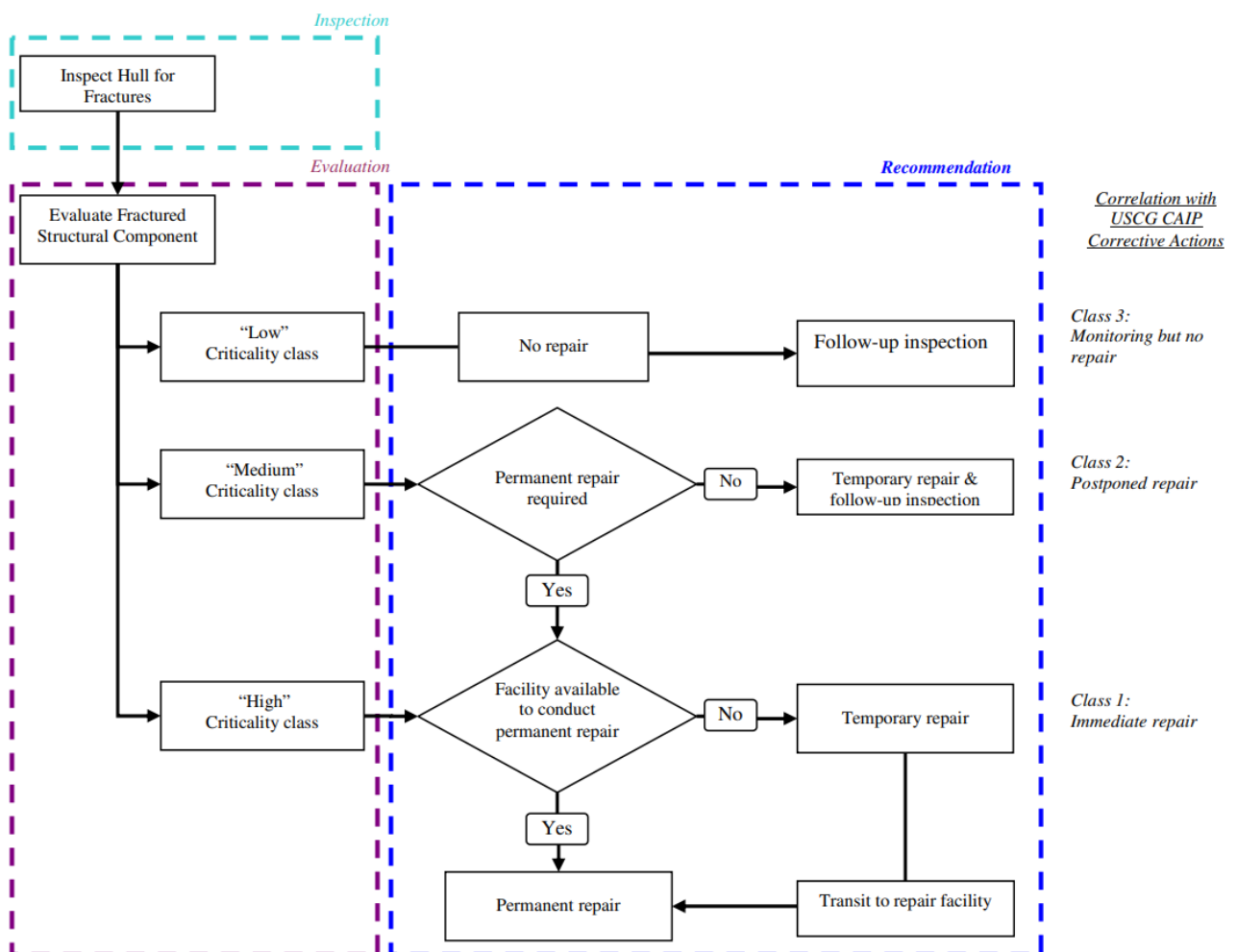
Figure 2: CAIP scheme for classing structural failures to guide reporting and corrective actions (figure adapted from [3])

Certain areas of the ship as shell plating, tanks (ballast, cargo, fuel), pipe duct space and cofferdams must remain watertight in order to ensure safe journey and undamaged cargo. Plates positioned at the contour of these areas contribute both to the ship's strength and its weathertightness & subdivision. When through cracks are detected then immediate repair is required, even if they are not expected to grow to its final size within the in-service inspection interval. So, these cracks are classified either as Class 1 or 2, as the one in Figure 3 (a). In contrast, other structural elements, such as stiffeners, girders, floors, stringers, web frames, inner platting in machinery and accommodation areas, etc..) only contribute to the ship's strength, and do not play any role in subdivision and watertighness of the ship. If a through crack is detected in these structural elements, it is permissible to assign Class 3 to it, as in Figure 3 (b).
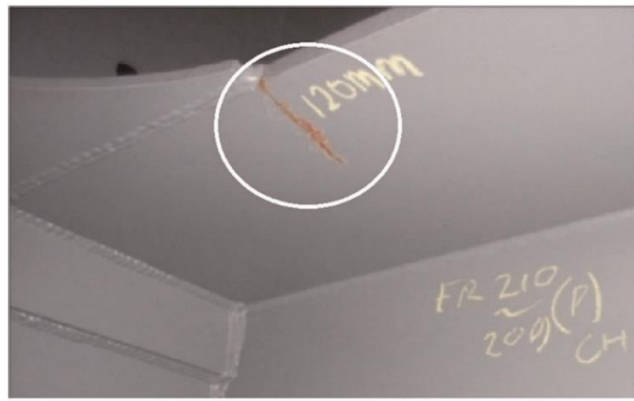
(a)   (b)

Figure 3: Examples of cracks is ship structures: a) a fatigue through crack in the inner bottom of a 15 year old pre-CSR Panamax bulk carrier classified as Class 1 and b) a fatigue crack in supporting member of a 5 year old pre-CSR Panamax containership classified as Class 2 or 3 [7].

To classify fatigue cracks according to the CAIP, it is necessary to evaluate the strength or serviceability of the ship and the affected main hull structural member [3]. When assessing a crack, a key parameter determined by rules and standards is the remaining useful life (RUL) which is the time until the crack growth becomes unstable leading to structural failure [5]. The determination of RUL requires probabilistic considerations due to the inherent uncertainties associated with fatigue crack propagation, which stem from uncertainties in materials and loading conditions.

While the RUL of a crack exhibits variability and uncertainty that may well be modeled with probabilistic methods, it is essential to assign a deterministic value to facilitate its classification and make decisions regarding repairs. To achieve a deterministic assessment, thresholds are introduced, effectively converting the problem from a probabilistic nature to a deterministic

framework, even if these thresholds tend to be conservative. This approach allows authorities to make binary decisions, indicating whether repair actions are required or not.

The introduction of thresholds serves the purpose of preventing failures and ensuring structural integrity until the subsequent inspection, aligning with the fundamental concept of "preventive maintenance." By employing conservative thresholds, authorities prioritize proactive measures aimed at mitigating potential risks and minimizing the likelihood of unforeseen failures. This proactive approach underscores the commitment to maintaining safety and reliability in maritime operations.

Unfortunately, unscheduled stops for repair lead to a significant financial hit for the shipowner. Such situations often lead to disruptions in the vessel's schedule, resulting in one or more days of travel delays, and subsequent losses in freight for vessels engaged in the spot market. For chartered vessels, these crack repairs may give rise to future claims by charterers. While the cost of repairs itself may not be as substantial as the aforementioned consequences, the owner still incurs considerable financial losses, often amounting to thousands of dollars.

From a risk management standpoint, when there exists a risk that a crack may reach its Remaining Useful Life (RUL) before the next scheduled repair, the most economically prudent course of action is to undertake the necessary repairs. This practice has become prevalent within the merchant shipping industry as it allows for financial equilibrium. In the context of dry docking, the repair costs may be significantly reduced as the vessel is already undergoing repair activities. However, these supplementary repairs can introduce further delays to the vessel's operation.

1.2. Bayesian HSM as predictive maintenance

Predictive maintenance can be viewed as a promising alternative to the prevailing assessment and repair practices for cracks in ships and marine structures. Monitoring and predicting the crack growth by using strain sensing, present a concept that enables classification societies to assess the crack's condition at any given time. With the ability to digitally inspect the crack in real-time, the binary decision of indicating whether repair actions are required can be deferred until later. So, when monitoring a crack length that corresponds to a risk of failure that is not tolerable, the classification society can decide ad hoc to increase the criticality class, and thus repair. In essence, the objective shifts from preventing failure until the next inspection to ensuring sufficient assurance that failure will be averted during subsequent voyages

Such an approach may considerably reduce the uncertainty contained in the problem and lead to better RUL predictions, thus reducing the need for unnecessary operational interruptions aimed at addressing crack repairs. Unfortunately, reducing unnecessary stops comes with a price, which is the cost of the sensors used in a crack growth SHM system. Presently, such a crack growth SHM falls short in terms of risk management compared to preventive maintenance. Nonetheless, with continuous advancements in technology and as the demand of strain sensors is expected to rise in the upcoming years [8], its cost is expected to be reduced, making crack SHM systems a more economically viable solution. Thus, crack detection, monitoring, and prediction through SHM offers a promising alternative to the traditional approach of assessing cracks through preventive maintenance.

The core concept of a crack Structural Health Monitoring (SHM) system revolves around monitoring and predicting crack growth. At the heart of this problem lies the crack length α, a key variable that requires monitoring and prediction. To effectively monitor the crack, strain sensors are strategically positioned near the crack tip, as further studied in Section 2.5. By leveraging the likelihood function, the strain measurements from these sensors at a point in time τ can provide an estimation of the crack length at that same moment. When it comes to predicting crack growth, a Bayesian inference scheme can be employed. This involves utilizing physical models, such as crack growth models, which leverage principles from physics to offer an initial crack growth prediction. These physical models are inherently probabilistic and are referred to as Prior models. Their predictions take the form of distributions known as prior distributions. By employing Bayes' theorem, the predictions from the prior models are compared to the estimations derived from incorporating the actual strain measurements into the likelihood function. The posterior distribution takes into account both sources of information and provides a comprehensive probabilistic description for the crack length, considering multiple facets. The posterior distribution also facilitates the update of beliefs or knowledge regarding the prior parameters, thus improving the physical model. In the subsequent step, the updated parameters can be employed to generate predictive distributions. Alternatively, the posterior distribution itself can now be treated as the updated prior for further iterations or analysis.

1.3.Thesis objectives

This thesis aims to develop two fundamental tools essential for the establishment of a predictive maintenance system for cracks in ships and marine structures. The first tool entails the development of an innovative fatigue assessment technique that integrates spectral analysis with stochastic crack growth models. Referred to as "Spectral Fatigue Analysis based on a Stochastic Crack Growth State Model", this technique constitutes the principal focus of this thesis. The latter fatigue assessment technique can be used for either cracked or intact structural elements of ships and marine structures, and can also be employed in the prior function estimation within a Bayesian framework for crack SHM. The second tool involves the formulation of a surrogate model, for the cracked structural element, by employing the finite element method (FEM). This tool can be utilized in the construction of the likelihood function used within a Bayesian framework for crack SHM, while at the same time it can support the sensor placement of the SHM. To demonstrate the practical application of those tools, a case study was conducted on the fatigue assessment and surrogate modeling of a cracked longitudinal girder that is assumed to be present on a 7800 TEU Very Large Container Ship (VLCS).

2. Theoretical background and formulation

In this chapter, the theoretical foundations of the technical portion of this thesis are presented. The chapter commences by introducing basic mathematical prerequisites, including Monte Carlo Simulation, Latin Hypercube Sampling and Bayesian Inference. Subsequently, a basic understanding of ocean engineering and ocean wave description is provided, as it is deemed essential to comprehend the proposed fatigue assessment technique. The chapter then proceeds to review the current state-of-the-art fatigue assessment techniques employed by shipping stakeholders, followed by presenting a comprehensive theoretical formulation of the proposed alternative method for fatigue assessment. Concerning the second tool developed in this thesis, the chapter finally provides an overview of the basic concepts and objectives related to sensor placement architecture. Readers interested in delving further into the topics covered are encouraged to explore the referenced sources encountered throughout this chapter.

2.1. Mathematical prerequisites

2.1.1. Monte Carlo Simulation

Monte Carlo simulation, named after the famous Monte Carlo casino in Monaco, is a widely utilized computational technique in various industries and academic fields. It provides a powerful approach to estimate probabilities and analyze complex probabilistic systems when analytical solutions are not feasible [9]. Monte Carlo simulation finds application in industries such as finance, risk management, engineering and physics. In this thesis, the focus lies on addressing physics-related problems in which the variables of interest are functionally related to other known quantities that possess inherent probabilistic properties. While the deterministic relationship between these variables is established, their probabilistic characterization lacks an explicit formulation. To tackle this challenge, Monte Carlo (MC) simulations are employed as a powerful computational tool.

The process of Monte Carlo simulation involves sampling the known probabilistic quantities, such as input parameters or variables, from their respective probability distributions. Each sampled case represents a particular combination of these quantities. Subsequently, the variables of interest are deterministically calculated based on the sampled values, utilizing the established functional relationships. This process is repeated for a large number of iterations, generating a collection of samples that collectively represent the probabilistic characteristics of the variables of interest.

Mathematically, suppose we have a set of known probabilistic quantities denoted as $X = \{X_1, X_2, ..., X_n\}$, where each X_i follows a specific probability distribution. The goal is to calculate the variables of interest $Y = \{Y_1, Y_2, ..., Y_m\}$, which are functionally dependent on X. The MC simulation involves the following steps:

- Sampling: Randomly sample values for each X_i from their respective probability distributions, generating a set of N samples. This results in an ensemble of input cases, where each case corresponds to a combination of sampled values for the input variables.

- Deterministic Calculation: Utilize the deterministic relationships between the variables of interest Y and the input variables X to calculate the values of Y for each sampled case. This involves performing the necessary computations, equations, or simulations based on the specific problem.

- Collecting Samples: As the deterministic calculations are carried out for each sampled case, the resulting values of Y are recorded. By repeating this process for N iterations, a collection of N samples representing the probabilistic characteristics of Y is obtained.

The Monte Carlo simulation provides an approximation of the statistical behavior of the variables of interest, enabling the analysis of their probabilistic properties. To ensure the convergence and reliability of this numerical method, the central limit theorem is often employed as a validating principle [9]. The central limit theorem states that as the number of samples increases, the distribution of the calculated variables tends to approach a Gaussian distribution. This property provides confidence in the accuracy and robustness of the MC simulation results.

2.1.2. *Latin hypercube sampling*

In addition to Monte Carlo simulations, this thesis also employs Latin Hypercube Sampling (LHS) as a sampling technique to enhance the probabilistic analysis. LHS is a method that provides a more efficient and representative sampling of the parameter space compared to pure random sampling.

In the context of the example presented in the above chapter, LHS is implemented by dividing the cumulative distribution function (CDF) of the random variable X_i into equal partitions or strata. Each partition represents a portion of the distribution's range. Within each stratum, a single random data point is selected based on the CDF of the X_i. This ensures that at least one value from each partition is included in the sample, resulting in a better representation of the overall distribution.

To illustrate this, consider Figure 4, where a small number of indicative samples drawn from a uniform distribution are displayed on the y-axis as blue dots. These samples are then transformed using the inverse CDF of the random variable X_i, into samples of X_i, noted as green points. By employing LHS, the samples are strategically distributed across the parameter space, minimizing clustering effects and providing a more even coverage.
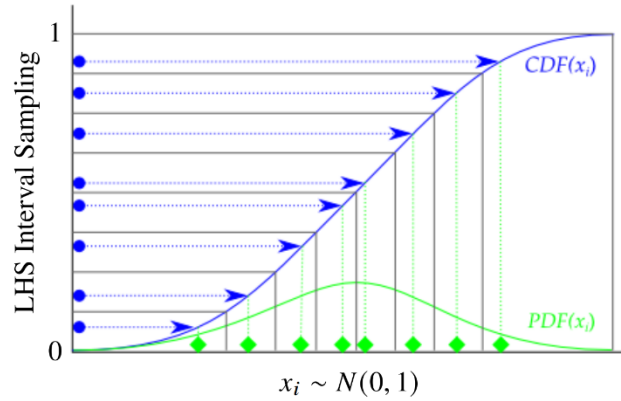
Figure 4: An example of LHS (figure adapted from [10])

The combination of LHS and Monte Carlo simulations allows for a comprehensive exploration of the probabilistic characteristics of the variables of interest. By leveraging LHS to obtain a well-distributed sample set and then performing the deterministic calculations based on each sampled case, the resulting collection of samples effectively captures the probabilistic behavior of the variables. This approach ensures that the MC simulation is not only statistically sound but also provides a robust representation of the system under investigation.

2.1.3. Bayesian inference for crack SHM

Bayesian updating in SHM offers a flexible and robust framework for combining prior knowledge with observed data, enabling more accurate and reliable estimation of model parameters or structural responses. It is particularly useful in scenarios where uncertainties are present, and continuous monitoring and updating are required to ensure structural integrity. This is especially evident in the context of fatigue.

In more specific terms, the likelihood function quantifies the probability of a sensor located in the point (x_i, y_j) to measure k-component strains $\varepsilon_{i,j}^k$ for given the crack length α. It can be constructed by utilizing a FEM based surrogated model SR, which returns a deterministic estimate of $\varepsilon_{i,j}^k$ given α. The sensor is anticipated to provide strain measurements accompanied by noise,

which can be effectively modeled as additive white noise represented by $N(0, I\sigma^2)$. So, the likelihood of measuring strain readings $\varepsilon_{i,j}^k$ is estimated:

$$p(\varepsilon_{i,j}^k \mid \alpha(\tau)) = SR(\alpha, x_i, y_j, k) + N(0, I\sigma^2) \qquad (1)$$

The prior distribution $p(\alpha(\tau))$ refers to the probability of a crack length α occurring at a particular time τ, considering no additional information. To obtain an estimate for this probability, it is necessary to construct a probabilistic physical model of the crack, such as the one formulated in 2.4.. The Bayes theorem can be applied as follows:

$$p(\alpha(\tau) \mid \varepsilon_{i,j}^k) = \frac{p(\varepsilon_{i,j}^k \mid \alpha(\tau)) \cdot p(\alpha(\tau))}{p(\varepsilon_{i,j}^k)} \qquad (2)$$

The marginal probability $p(\varepsilon_{i,j}^k)$ is the same for all possible hypotheses being considered and hence does not factor into determining the relative probabilities of different hypotheses. So, from the Bayes theorem the following relation can be obtained:

$$p(\alpha(\tau) \mid \varepsilon_{i,j}^k) \propto p(\varepsilon_{i,j}^k \mid \alpha(\tau)) \cdot p(\alpha(\tau)) \qquad (3)$$

in order to estimate the posterior distribution $p(\alpha(\tau) \mid \varepsilon_{i,j}^k)$, as also depicted in Figure 5. The latter can be utilized to update beliefs over both the crack length and the parameters of the physical model used as prior.
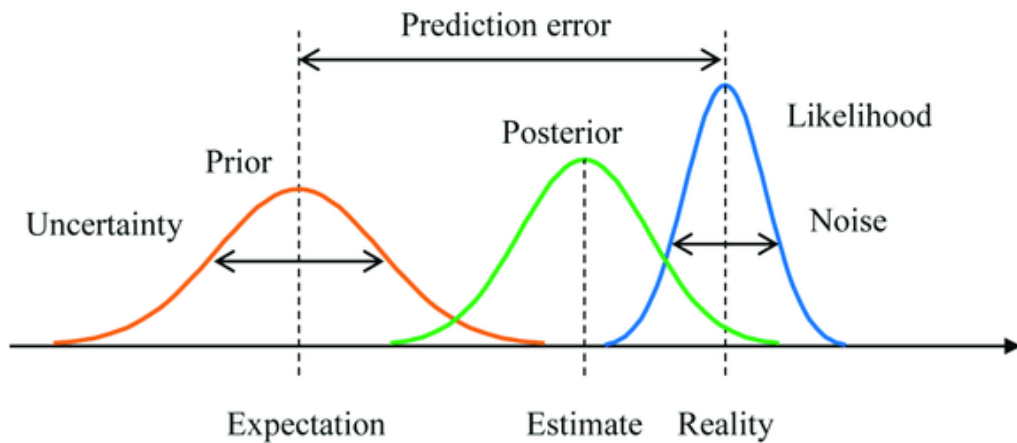
Figure 5: Bayesian inference (figure adopted from [11])

2.2.Ocean engineering prerequisites

This section provides an overview of the probabilistic modeling approach employed by ocean engineers to describe ocean waves, presenting simplified concepts for enhanced reader comprehension. The fundamental physical quantities observed in the marine environment are defined along with their corresponding statistics, such as the significant wave height and zero up-crossing period. The concept of the sea state is explained, and its duration is quantified. A commonly used model that describes the observed quantities by utilizing their statistics within a particular sea state is presented. Additionally, the basic spectral concepts and quantities, such as the wave spectrum, are defined. Finally, it is demonstrated how oceanographers probabilistically model regional statistics that are characteristics of a sea state, though wave scatter diagrams.

2.2.1. *Observed and statistical quantities of ocean waves*

Ocean waves encountered in seas, referred to as total seas, arise from the combination of diverse wave systems such as wind seas, swells, etc., under the assumption of linearity [12]. The resultant wave behavior is inherently stochastic in nature. Consider the recording of the free surface elevation $\eta(x, \tau) = \eta(x_0, \tau)$ where $x_0 = (x_1, x_2)$ represents a fixed point on the undisturbed free surface, and τ denotes the time, as further elucidated in reference [13]. The recording consists of an irregular sequence of crests and troughs, corresponding to local maxima and local minima of the wave surface elevation, as illustrated in Figure 6. Possible local ripples that appear are usually disregarded. Based such a recording, the following quantities are defined:
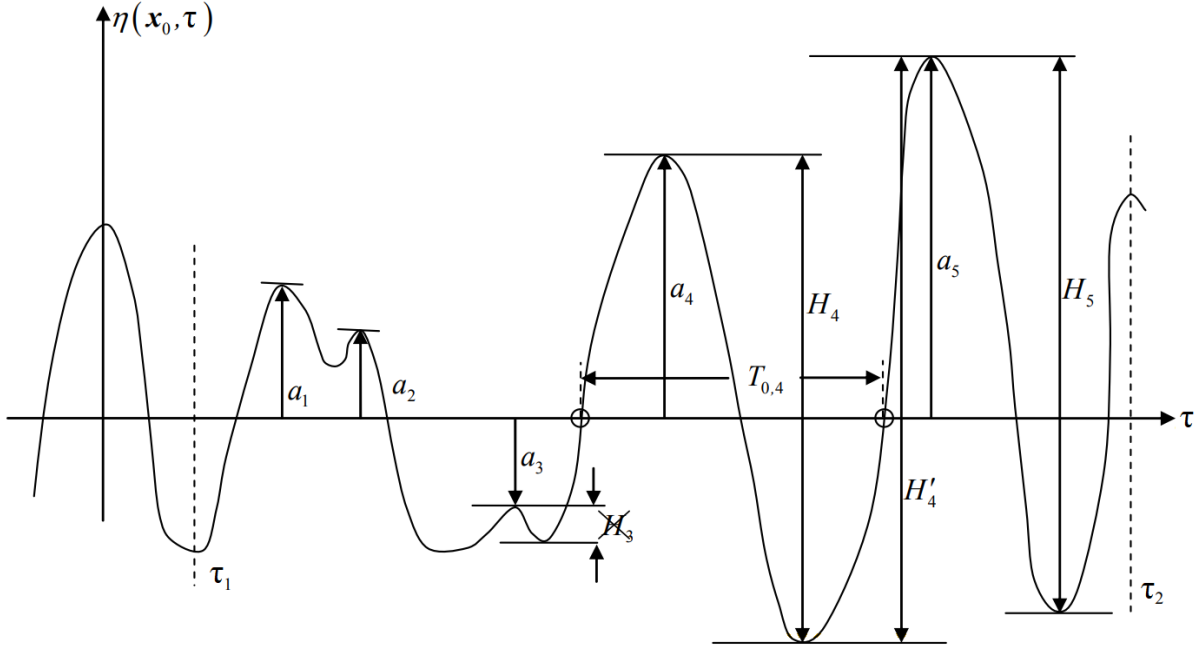
Figure 6: A typical recording of a wave surface elevation (figure adopted by [13])

- The observed wave height H refers to the (absolute) vertical distance between a crest and the subsequent trough (e.g., H_4 in the figure).

- The observed zero up-crossing period T_0 represents the time interval between two consecutive crossings of the undisturbed level by the function $\eta(\tau)$.

By analyzing the sea surface elevation within a specified time window $\Delta\tau$, a sequence of observed wave heights can be obtained $\{H_1, H_2, H_3 ... H_r ... H_R\}$. This sequence can be arranged in descending order from the highest to the smallest wave heights, denoted as 1 to R, respectively. If we consider this ordered sequence of wave heights as a distribution, we can define the following statistical quantities:

- The significant wave height H_S is the average height of the waves that are larger than approximately one third of all the waves observed or measured in the recording during the specified time window:

$$H_S = \frac{1}{R/3} \sum_{r=1}^{R/3} H_{r:R} \qquad (4)$$

- The significant zero up-crossing period T_0 is the average of the zero up-crossing periods that correspond, one by one, to the larger one third portion of the wave heights above.

2.2.2. *The concept of a sea state*

Let's assume that we have a continuous recording of the sea surface elevation over a long period of time, similar to the one illustrated in Figure 6. It is evident that the recorded waves vary in intensity, ranging from strong to mild, and there are also periods of calmness. Therefore, the computed significant wave height will differ depending on the time window for which it was calculated. In other words, the statistical quantities of the ocean waves are not constant but change, albeit at a much slower pace than the free surface elevation and the observed wave quantities [12]. To quantify this, the concepts of sea state and the duration of the sea state are defined. So, a specific sea state is characterized by the fact that, during its duration stationarity is met, meaning that fluctuations of the statistical quantities H_S and T_Z vary more slowly than the observed quantities, H and T_0 accordingly. The duration of a sea state $\Delta\tau_{SS}$ ranges from 1-2 hours to 1-2 days (in oceanic contexts), with average values ranging from 3 to 6 hours [13]. Consequently, the sea state remains practically stable for a period of up to 3 hours (and up to 6 hours in open seas) [13].

From now on, when referring to the significant wave height H_S and zero up-crossing period T_Z it is implicitly understood that these statistical measures are computed within a time window that aligns with the duration of a specific sea state $\Delta\tau_{SS}$. For that reason, they will be referred to as the significant wave height H_S and zero up-crossing period T_Z of a particular sea state, thus describing the statistical quantities of a sea state in general. In general, the probabilistic description of the observed quantities within a particular sea state will be referred to as short-term statistics for the scope of this work.

2.2.3. *Short-term statistics*

Ocean engineers have developed models based on the Rayleigh distribution to describe the sequence of observed quantities within a sea state, with certain short-term statistics serving as parameters. These models are explained in detail in reference [6]. Additionally, a more modern approach involves utilizing spectral analysis, as mentioned in the same reference [6]. Within a sea state, the wave spectrum represents the distribution of wave energy across different wave frequencies, denoted by ω [14]. Ocean engineers have formulated various models for these wave

spectra, where the short-term statistics of a sea state are used as parameters. Examples of such models include the Johnswap spectrum, the Pierson-Moskowitz spectrum, the Bretschneider spectrum, and others. The *p*-th order moments, denoted as m_p, of these spectra can be employed as parameters for the Rayleigh distribution, rather than directly utilizing the short-term statistics themselves. Such a Rayleigh distribution can be used as the probability density function of the observed wave height as illustrated in reference [6]:

$$H = \frac{2H}{\left(f\left(m_0, m_1, m_2\right)\sqrt{8m_0}\right)^2} \exp\left[\frac{H^2}{f\left(m_0, m_1, m_2\right)\sqrt{8m_0}}\right] \tag{5}$$

2.2.4. Long-term statistics

Let's consider again the recording of the wave surface elevation of Figure 5. The recording can be segmented into time windows $\Delta\tau_{SS}$ corresponding to stationary sea states. Within each of these time windows, denoted as sea states, the statistical quantities defined above H_S and T_Z are calculated. Consequently, a sequence of these statistical quantities H_S and T_Z is obtained. This resultant sequence can be further transformed into a joint histogram, representing the distribution of the (H_S, T_Z) pairs, and it is characteristic for the $x_0 = (x_1, x_2)$ point of recording. By performing this procedure for various points within a specific area, the individual histograms can be combined to generate a comprehensive wave scatter diagram, as illustrated for the North Atlantic region in Table 1. The probabilistic description of the statistical quantities, such as H_S, T_Z, will be referred to as long-term statistics for the scope of this work.

Wave Height (m)*		Wave Period (sec)**											Sum Over All Periods
		3.50	4.50	5.50	6.50	7.50	8.50	9.50	10.50	11.50	12.50	13.50	
	0.5	8	260	1344	2149	1349	413	76	10	1			5610
	1.5		55	1223	5349	7569	4788	1698	397	69	9	1	21158
	2.5		9	406	3245	7844	7977	4305	1458	351	65	10	25670
	3.5		2	113	1332	4599	6488	4716	2092	642	149	28	20161
	4.5			30	469	2101	3779	3439	1876	696	192	43	12625
	5.5			8	156	858	1867	2030	1307	564	180	46	7016
	6.5			2	52	336	856	1077	795	390	140	40	3688
	7.5			1	18	132	383	545	452	247	98	30	1906
	8.5				6	53	172	272	250	150	65	22	990
	9.5				2	22	78	136	137	90	42	15	522
	10.5				1	9	37	70	76	53	26	10	282
	11.5					4	18	36	42	32	17	7	156
	12.5					2	9	19	24	19	11	4	88
	13.5					1	4	10	14	12	7	3	51
	>14.5					1	5	13	19	19	13	7	77
Sum over All Heights		8	326	3127	12779	24880	26874	18442	8949	3335	1014	266	100000

Table 1: ABS North Atlantic Wave Scatter Diagram for Unrestricted Service Classification (table adapted from [15])

2.2.5. Response Amplitude Operators

The preceding paragraphs provide detailed insights into the modeling of ocean waves. Within the scope of this thesis, ocean waves are examined as a loading phenomenon, with a specific focus on their interaction with the ship's structure and the resulting induced stresses. The dynamic response of the ship is described by the time functions of various ship motions (roll, pitch, yaw, surge, sway, heave), which are influenced by the encountered wave and the hull geometry [13]. When designing a vessel, complex transfer functions known as Response Amplitude Operators (RAOs) are commonly constructed, as furtherly explained in [13], linking the wave amplitude to the ship motion amplitudes as a function of the wave frequency. This process entails the development of a hydrodynamic model for the ship. Delving further, the structural response of the ship is described by the time functions of e.g. bending moments, torsional moments, or stress at hot spot areas. These quantities depend on factors such as the encountered wave, hull geometry, and ship

structure. To construct bending moment and stress RAOs, both structural and hydrodynamic models of the ship need to be established.

A typical $RAO_\sigma(\omega, \theta)$ for the stress at a point of interest on the structure of a merchant ship is depicted in Figure 7 with the heading angle θ as parameter. Consider a sinusoidal wave of amplitude $a = H/2$ and frequency $\omega = 2\pi/T_0$ encountering the ship at a heading angle θ. Assuming a linear process, the stress at the point of interest is also a sinusoidal function with an amplitude of $\sigma = RAO_\sigma(\omega, \theta) \cdot a$ and frequency ω.
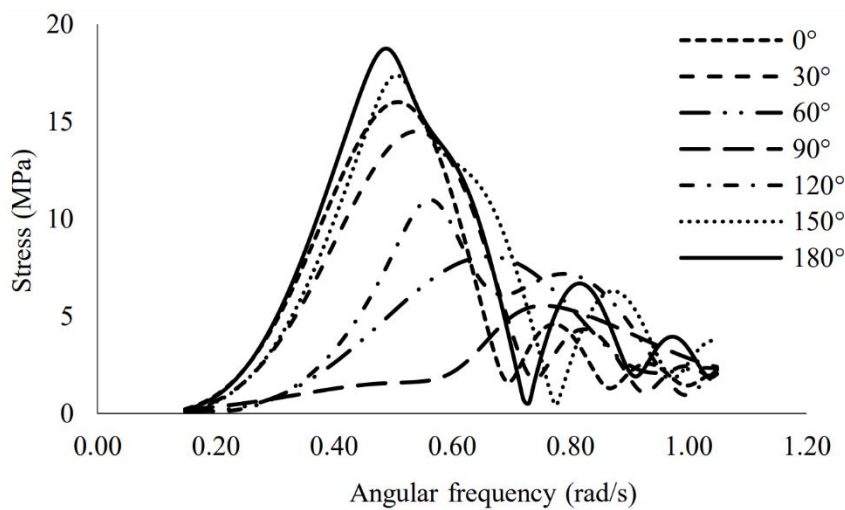
Figure 7: Stress RAO of a structural detail (figure adapted from [16])

In order to get a better intuition on Figure 7, consider the following example which investigate the Vertical Bending Moment (VBM) and the primary stresses induced by heading waves of varying frequencies on a vessel. When encountering a low frequency wave, the ship exhibits a buoy-like response, characterized by a heave motion with an amplitude equal to that of the wave. In this scenario, where the wavelength of the wave is greater than the ship's length, the pressure remains constant across all points on the Flat of Bottom (FOB) at a specific moment in time. Consequently, no Vertical Bending Moment (VBM) is induced, resulting in the absence of primary stresses, as depicted in Figure 8 (a). On the other hand, with moderate-frequency waves, the ship responds with a heave motion of a different amplitude compared to the wave. As the wavelength becomes comparable to the ship's length, the pressure at the FOB induces a non-zero VBM and subsequent primary stresses as depicted in Figure 8 (b). In the case of high-frequency waves, where the ship length is significantly greater than the wavelength, the wave pressures in the FOB counterbalance

each other, resulting in a zero total VBM and subsequent primary stresses at a specific moment in time, as in Figure 8 (c).

Low wave frequency (ω) **Moderate wave frequency (ω)** **High wave frequency (ω)**

VBM=0 **VBM≠0** **VBM=0**
No primary stresses induced **Primary stresses induced** **No primary stresses induced**

(a) (b) (c)
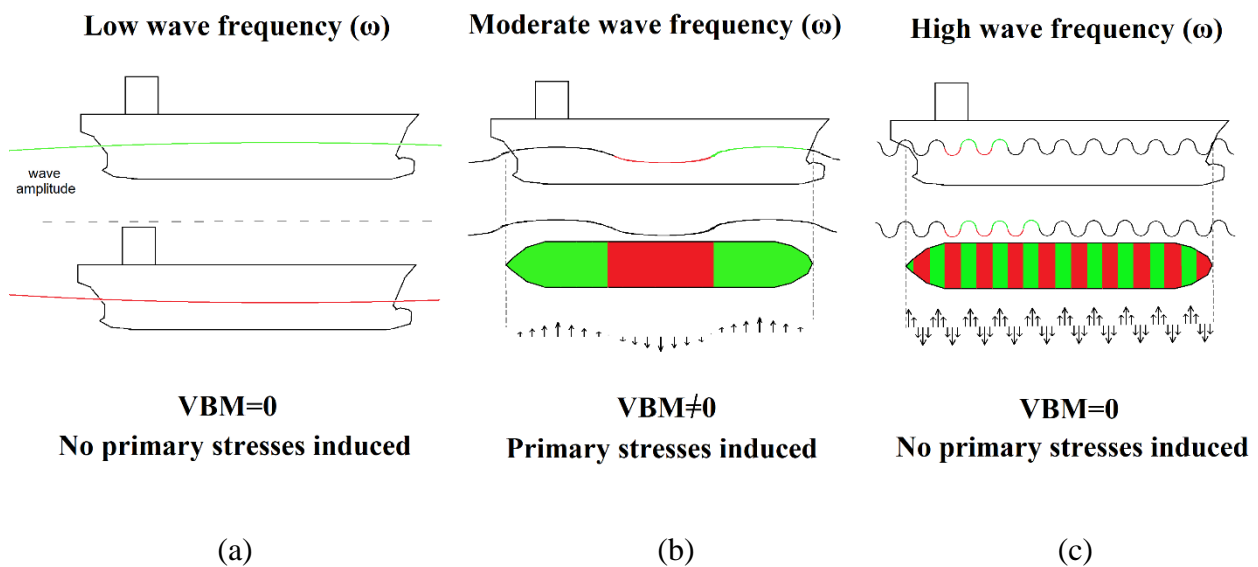
Figure 8: Ship encountering waves of low (a), moderate (b) and high (c) frequency

2.3. Fatigue assessment: State of the art

Fatigue is one of the most common modes of failure and damage mechanisms. It is a damage process whereby embedded or surface cracks can initiate and grow under fluctuating stress e.g. due to applied loads, thermal stress variations and vibrations. Fatigue cracking of ship hulls, and marine structures in general, is primarily caused by repeated loads originating from ocean waves, which are stochastic per se. In addition to the cyclic stresses caused by wave forces, fatigue fractures are also caused by vibration forces derived from main engine(s) or propeller(s), especially in the aft-most part of the hull. However, as these cases occur less often, this chapter and thesis focus on fatigue driven solely by ocean waves.

There are two main quantities of interest while assessing the fatigue accumulation of a ship structural element depending on the situation. On the one hand there is the total fatigue life (TFL), which is the total time between the ship's commissioning and structural failure due to fatigue, that is of primary interest during the design process. On the other hand, when assessing the fatigue accumulation of a cracked structural element for an existing ship, the main quantity of interest is the remaining useful life (RUL). In order to estimate the TFL or RUL, information about the developed stresses on the structural element is required. Depending on how the uncertainty in

26

fatigue loading is modeled, fatigue assessment techniques may fall under the so-called spectral analysis or simplified method categories [17], which will be elaborated more below. Another significant distinction of fatigue assessment techniques is the method by which fatigue damage is assessed. Namely, fatigue assessment techniques can be distinguished based on whether they employ SN curves along with the Palmgren-Miner rule to quantify damage accumulation or fatigue crack growth (FCG) models that are typically based on fracture mechanics (e.g., the Paris-Erdogan law [18], NASGRO [19] etc.). The most common techniques found in the literature combine either the spectral fatigue analysis along with SN curves [20], [21] or the simplified method along with FCG models [22], [23].

In spectral analysis, various orders of spectral moments of the applied stress are obtained by performing a first principles-based seakeeping analysis and subsequent mathematical manipulations [24]. Using the spectral moments, the Rayleigh probability density function describing the short-term stress range distribution and the zero-up crossing frequency of the stress response is then calculated [15]. In most relative research, fatigue damage is modeled utilizing S-N curves and the Palmgren-Miner rule is employed to estimate TFL or RUL [25], [26], [27]. In such cases, the total fatigue damage of a structural element is calculated by adding up the short-term damages accrued over all the applicable sea states in a specific wave scatter diagram. Therefore, the spectral method can account for various sea states together with their corresponding probability of occurrence [17]. However, this approach fails to account for the sequence according to which the structures encounter wave loads. In this thesis, it is demonstrated that the sequence has a significant impact on fatigue life, and we develop a robust framework that quantifies the associated uncertainty. Furthermore, the Palmgren-Miner rule lacks a clear definition of failure, as the fatigue capacity has no physical interpretation, in contrast to FCG methods where failure is clearly defined.

Employing FCG models to describe fatigue damage can be viewed as a promising alternative to the SN curves [28]. The employment of such models in calculating the RUL of an operating ship's cracked structural elements is straight forward, as the identified crack size is used as the initial crack size in the method [5]. Crack size identification can be achieved through the use Structural Health Monitoring (SHM) techniques, which are able to provide updated information based on structural response data, therefore further quantifying and reducing uncertainty [29], [30], [31]. In contrast, estimating the TFL of an under-design ship's intact structural elements using FCG models is discouraged by rules-based standards [32]. The main pitfall is the accurate quantification of an

equivalent initial flaw size (EIFS), which also contains high uncertainty and therefore needs to be assumed either deterministically or probabilistically [33]. Apart from EIFL magnitude, additional model parameters such as material related parameters and loading descriptors also contain significant uncertainty. To account for this, FCG models can be cast in a probabilistic setting allowing for uncertainty quantification in the estimates of the fatigue life. Stochastic FCG methods that can be utilized for this task are based on Monte Carlo Simulation (MCS), where different realizations of the model's stochastic parameters are generated and used in order to estimate an empirical distribution of TFL or RUL. Most relative research efforts employ the simplified method to describe uncertainty in the FCG parameters, according to which the long-term stress range distribution of a ship structural element is assumed to follow a known distribution [22], [23], [34] usually a Weibull as indicated in [6]. However, it is tricky to estimate such a distribution in marine structures as the fatigue loading primarily originates from ocean waves that are stochastic in nature.

To address the above challenges, a method is proposed in this work in Section 2.4 which employs a time discretization scheme to define temporal intervals, corresponding to sea states, where the marine environment, and therefore the fatigue loading, is assumed to be constant. This approach allows for the use of stochastic FCG models to describe the evolution of fatigue damage within each sea state for different realizations of the model parameters, using the fatigue loading parameters (stress range and number of cycles), obtained as a result of the spectral analysis. To the author's knowledge, this approach has been illustrated so far only for deterministic FCG models in [35], [36] and is herein extended for the first time to a probabilistic setting.

2.4. Spectral fatigue analysis based on a stochastic crack growth state model

In this section, key theoretical considerations regarding the proposed methodology will be presented. First, the particulars of spectral fatigue analysis, as applied to ship structures, will be detailed. This will be followed by a discussion on using stochastic fatigue crack growth models to obtain probabilistic estimates of quantities of interest related to fatigue life. The flowchart presented in Figure 9 provides an overview of the proposed method.
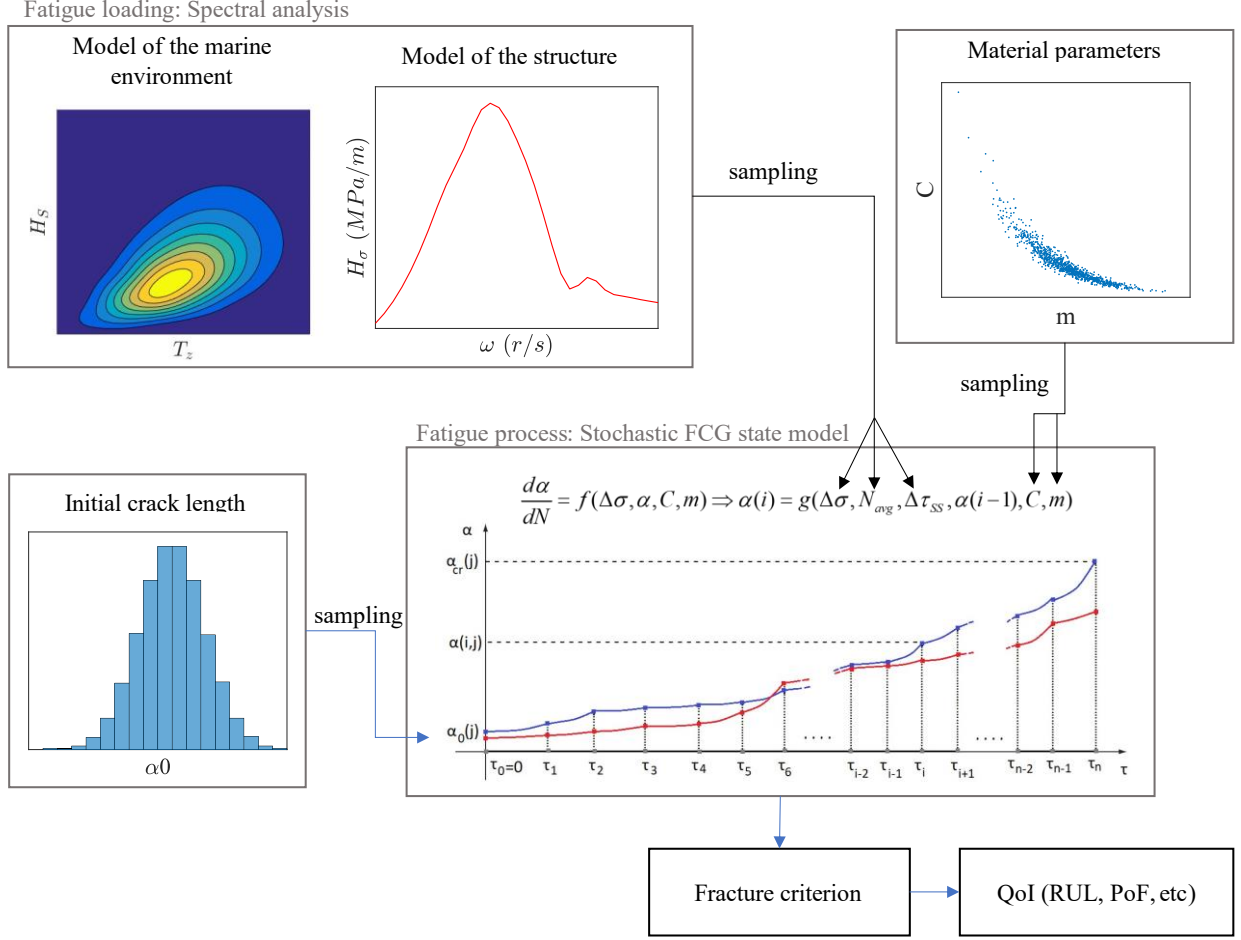
Figure 9: Flowchart of the spectral fatigue analysis method based on a stochastic crack growth state model.

2.4.1. *Spectral fatigue analysis*

To effectively translate the understanding of the marine environment into an understanding of the structural response, characterized here by the stress range, it is imperative to develop a spectral description that characterizes both variables. The wave spectrum $S_\eta(\omega)$, which represents the distribution of wave energy in the frequency domain, is often described using sea state statistics such as H_S and T_Z [24]. Therefore, constructing the wave spectrum requires separate consideration for each particular sea state. The stress transfer function $H_\sigma(\omega)$ relates the amplitude of a sinusoidal wave that is encountered by a ship to the amplitude of the sinusoidal stress response. This response can be constructed using hydrodynamic and structural analysis of the detail of interest. The stress spectrum $S_\sigma(\omega)$, which represents the distribution of fatigue loading energy in the frequency domain, can be estimated by combining the knowledge of the

wave spectrum $S_\eta(\omega)$ and the stress transfer function $H_\sigma(\omega)$. Finally, the stress spectrum is translated back to long-term statistics of the stress range for a particular sea state, sufficiently describing the structure's fatigue loading.

❖ *Stochastic modeling of the marine environment*

A marine structure is expected to experience various sea states sequentially throughout its lifetime, with each sea state noted as here an i case, where $i \in \mathbb{Z}^{0+}$. According to the description provided earlier, the duration of each particular sea state $\Delta\tau_{SS}$ can be modeled as a random variable. Accordingly, the operational life of a vessel can be discretized into intervals comprised of individual sea states thus leading to a recursive relation of the following form:

$$\tau(i) = \tau(i-1) + \Delta\tau_{SS}(i) \tag{6}$$

where the reference time $\tau(i=0)=0$ corresponds to either the ship's commissioning for an under-design ship, or to the moment when the crack was detected for an operating vessel. A schematic representation of the time-discretization scheme is provided in Figure 10. Each sea state will be characterized by a specific $H_S(i)$, $T_Z(i)$ pair which can be sampled across various sea states according to their joint probability distribution, depending on the structure's operational profile as illustrated in Figure 9. A wave spectrum $S_\eta(\omega \mid H_S(i), T_Z(i))$ can then be calibrated for $H_S(i)$ and $T_Z(i)$, respectively, and then used in order to perform spectral analysis for each sea state. Ultimately, the wave spectrum $S_\eta(\omega)$, the joint distribution $p(H_S, T_Z)$ and the sea state duration $\Delta\tau_{SS}$ are capable of adequately describing the marine environment in the long-term, and as such form the basis of spectral fatigue analysis.
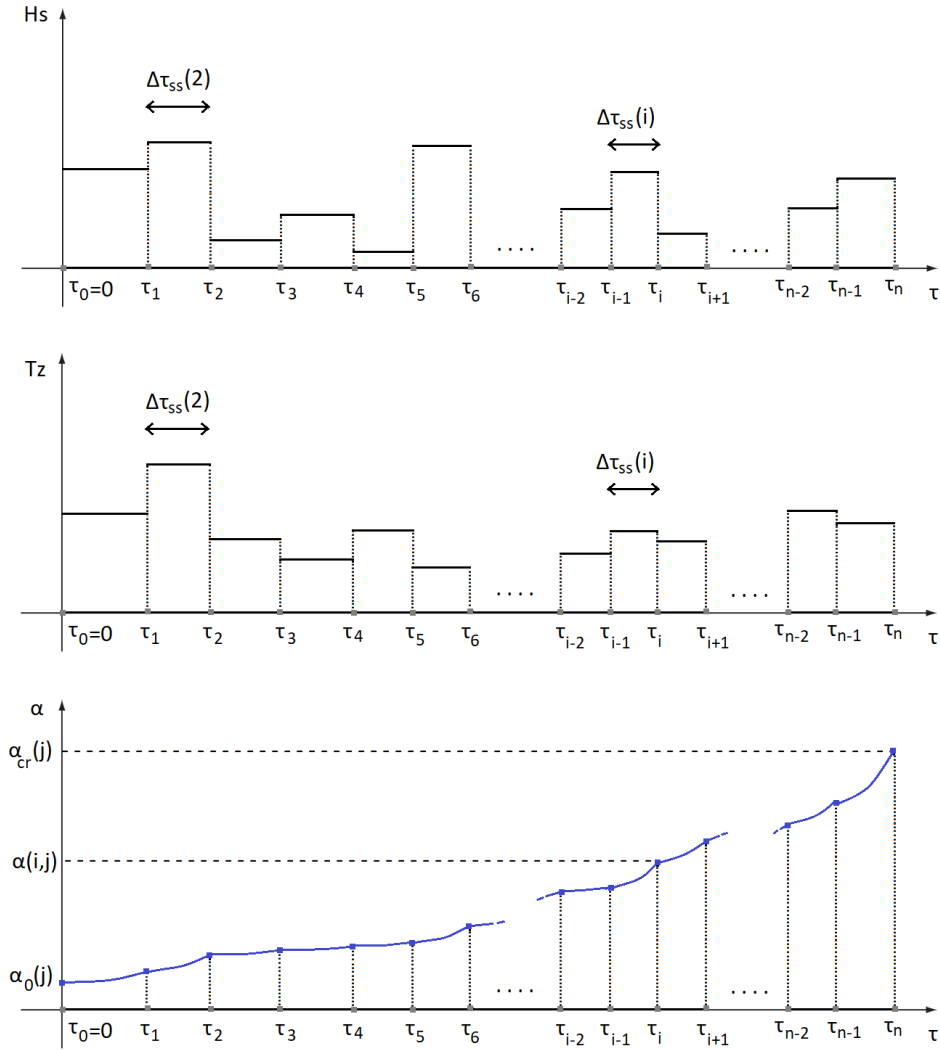
Figure 10: Time-discretization scheme of vessel operational life into individual sea states (a) and application of a fatigue crack growth model within each sea state interval (b).

❖ *Structural system model*

In order to estimate the spectral response of the structure within a sea state, the stress transfer function $H_\sigma(\omega)$ needs to be calculated. The structural system is assumed to be linear, e.g. when encountering a given sinusoidal wave, a corresponding sinusoidal stress response is observed at the designated point of interest. To quantify this function, it is necessary to create both a hydrodynamic and a structural model of the structure. The hydrodynamic model is constructed using constant amplitude sinusoidal waves as inputs, which produce a pressure field at the boundary of the structure. This pressure field is then used as input to a global structural model, which provides the boundary conditions for a local structural model. The latter is subsequently

used to calculate the stress amplitude. By performing this analysis for various wave frequencies ω, heading angles θ, and loading conditions LC, it is possible to construct the stress response amplitude operator (RAO) $RAO_\sigma(\omega|\theta,LC)$, which corresponds to the amplitude of the sinusoidal stress function induced by a 1-meter amplitude sinusoidal wave. The stress transfer function is then defined as:

$$H_\sigma(\omega,\theta,LC) = \left| RAO_\sigma(\omega|\theta,LC) \right| \tag{7}$$

The heading angle θ and loading condition LC are modeled as random variables depending on the marine structure type of interest and its operational profile.

❖ *Stress response spectrum*

The stress response spectrum can be calculated by the wave spectrum and the stress range transfer function, for each sea state, as follows [15]:

$$S_\sigma(\omega|\theta,LC,H_S,T_Z) = H_\sigma^{\ 2}(\omega;\theta,LC) \cdot S_\eta(\omega|H_S,T_Z) \tag{8}$$

The *p*-th spectral moment of the response spectrum, is calculated as follows:

$$m_p = \int_0^\infty (\omega - V_S \omega^2 \cos\theta/g)^p \cdot S_\sigma(\omega)\,\mathrm{d}\omega, \ p=1,2,3... \tag{9}$$

where V_S denotes the ship's speed and g refers to the gravitational acceleration. The Rayleigh distribution is suitable to describe the short-term wave height H [37]. So, the stress range at the point of interest $\Delta\sigma(i)$ can also be assumed to follow a Rayleigh distribution across a sea state as well, with a scale parameter $\sigma = 2\sqrt{m_0}$ [15], and thus its probability density function is:

$$\Delta\sigma(s) = \frac{s}{\left(2\sqrt{m_0}\right)^2} \exp\left[-\frac{s^2}{4 \cdot 2\sqrt{m_0}} \right] \tag{10}$$

As the stress range distribution is known for each sea state, a further subdivision of the sea state in even smaller time spaces, where each has an assigned wave height H is possible. Although, as this would increase significantly the computational cost an equivalent constant short-term stress range $S(i)$ is assumed to be the mean of the above Rayleigh distribution $S(i) = \overline{\Delta\sigma(i)} = \sqrt{2\pi m_0}$ [15]. The zero up-crossing frequency of the stress response is assigned to a deterministic value

$N_{\text{avg}}(i) = \sqrt{m_2/m_0}/2\pi$ within each sea state [15]. In other words, all variables are assumed to be constant in the short-term.

As fatigue loading is assumed to solely originate from ocean waves encountered by the ship, the fatigue loading pair $\langle S(i), N_{\text{avg}}(i) \rangle$, is sufficient to describe the fatigue loading during the i-th sea state with duration $[\tau(i-1), \tau(i)]$. So, the pairs of data S, N_{avg} consist of all the values that these variables may take throughout time. The order by which $S(i)$ and $N_{\text{avg}}(i)$ occur across sea states is random as it is a result of random H_S, T_Z sampling across sea states. Ultimately, the resulting pairs of data corresponding to S, N_{avg} and τ can be viewed as the expected fatigue loading history matrix of the structure. The flowchart of the fatigue load estimation technique is presented in Figure 11.
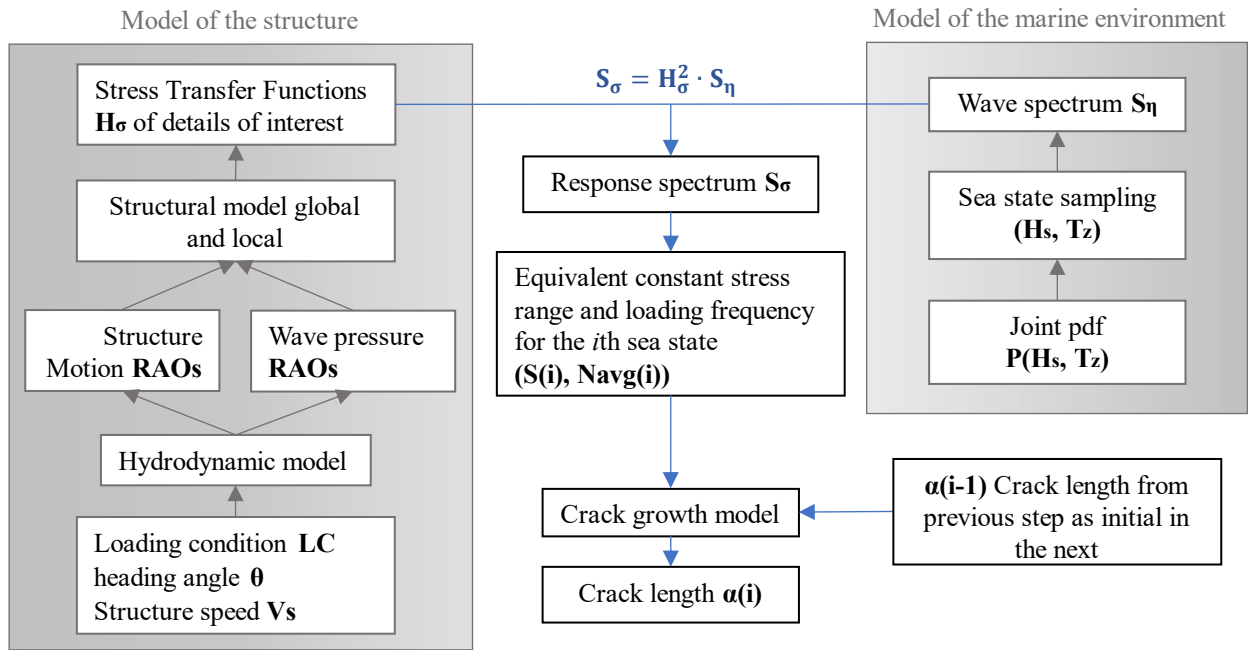

Figure 11: Flowchart of the proposed fatigue load estimation technique.

2.4.2. Crack growth model

Crack growth during a particular sea state is modeled by a law of the form $da/dN = f(\Delta\sigma, \alpha)$, such as Paris law, NASGRO etc. The FCG model is solved within each sea state, as fatigue loading remains constant during that time, as schematically shown in Figure 1b. During the i-th sea state, the crack has propagated for a length $\alpha(i)$ which can be determined as follows:

$$\frac{d\alpha}{d\tau} = N_{avg} \cdot f(\Delta\sigma, \alpha) \Rightarrow \int_{\alpha(i-1)}^{\alpha(i)} \frac{d\alpha}{f(\Delta\sigma, \alpha)} = \int_{\tau(i-1)}^{\tau(i)} N_{avg} d\tau \Rightarrow \alpha(i) = g(\Delta\sigma, N_{avg}, \alpha(i-1), \Delta\tau_{SS})$$

$$(11)$$

where $\alpha_{i=0}$ is the initial crack size. The crack length $\alpha(i)$ that has propagated over time $\tau(i)$ describes one crack growth path. The initial crack size α_0 is treated as a random variable due to the uncertainty of EIFS when referring to intact plates (design phase) and due to measuring errors when referring to cracked plates. The material parameters included in the crack growth formula f are treated as random variables as well, because of the high uncertainty over the microstructure of metals. Similarly, the expected fatigue loading history is treated as a random matrix. For each realization of the above random parameters, a different crack growth path occurs, denoted here as a crack growth trajectory and associated in the notation with the index $j \in \mathbb{Z}^+$.

Fracture resistance can be estimated by either a critical crack length criterion, denoted here as C1, or a critical crack growth rate criterion, denoted here as C2, or potentially both. The RUL of a structural element is reached, according to C1, when a particular crack at a specific moment in time, denoted here as $\alpha(\tau)$, exceeds a predefined deterministic critical crack length α_{cr} or according to C2, when the crack growth rate $\dfrac{d\alpha(\tau)}{d\tau}$ exceeds a predefined deterministic critical value $\dfrac{d\alpha(\tau)}{d\tau}\bigg|_{cr}$. When using both criteria, the RUL can be defined as the earliest time instant when either C1 or C2 is satisfied. The above critical values depend on the risk tolerance of the ship's management. Applying one of these criteria to one crack growth path leads to a single estimation of the RUL. So, when performing this analysis for j crack growth trajectories a distribution of the RUL is obtained. Algorithm 1 presents a generic illustration of the proposed method for the estimation of the RUL distribution.

Algorithm 1: Calculation of RUL using a stochastic FCG state model
---

for j=1, …, K

      sample $\alpha_0(j)$, $C(j)$, $m(j)$

      $\tau(0) = 0$

      for i=1,… ,n

            sample $H_S(i,j)$, $T_Z(i,j)$, $\Delta\tau_{SS}(i,j)$

            $\tau(i,j) = \tau(i-1,j) + \Delta\tau_{SS}(i,j)$

            calculate $S_\eta(\omega,i,j)$, $S_\sigma(\omega,i,j)$, $S(i,j)$, $N_{avg}(i,j)$

            $\alpha(i,j) = g(\Delta\tau_{SS}, C, m, S, N_{avg}, \alpha(i-1,j))$

            if C1 or C2 true **then break**

      end

      $RUL(j) = \tau(i-1)$

end

In order to assess the probability of fracture (equivalent to the well-known probability of failure in the field of structural reliability) $PoF(\tau)$ at a given point in time τ, while a C1 type criterion is solely utilized, α_{cr} is treated as random variable. The probability of fracture is described as $PoF(\tau) = P(\alpha_{cr} - \alpha(\tau) \leq z)|_{z=0}$ where the subtraction probability is calculated by integrating the convolution of the subtracted RVs' distributions [38]. As α_{cr} and $\alpha(\tau)$ are independent variables, their joint distribution is simply equal to the product of the two marginal distributions, thus the convolution's integral becomes:

$$PoF(\tau) = \int\limits_{-\infty}^{0} \int\limits_{-\infty}^{+\infty} f_{\alpha(\tau)}(\alpha_{cr} - z) \cdot f_{\alpha_{cr}}(\alpha_{cr}) d\alpha_{cr} dz \tag{12}$$

where $f_{\alpha(\tau)}$ and $f_{\alpha_{cr}}$ are the probability density functions (PDFs) of $\alpha(\tau)$ and α_{cr} respectively. As the results of the method are the $\alpha(\tau)$ and α_{cr} distributions, the PDFs are estimated by the

empirical PDFs (ePDFs) produced by these results. The $PoF(\tau)$ can be calculated, using numerical methods, by the following integral:

$$PoF(\tau) = \int\limits_{z_{min(\tau)}}^{0} \int\limits_{a}^{b} ePDF_{\alpha(\tau)}(\alpha_{cr} - z) \cdot ePDF_{\alpha_{cr}}(\alpha_{cr}) d\alpha_{cr} dz \tag{13}$$

where:

- $a = \max(\min(\alpha_{cr}), \min(\alpha(\tau) - z))$,

- $b = \min(\max(\alpha_{cr}), \max(\alpha(\tau) - z))$, and

- $z_{min}(\tau) = \max(\max(\alpha(\tau) - z) - \min(\alpha_{cr}), 0)$.

A similar process could be followed for calculating the probability of fracture when a C2 type criterion is utilized.

2.5. Sensor placement architecture

Sensor placement architecture refers to the overall design and framework used to determine the locations for placing sensors in a system or structure. It encompasses the methodology, algorithms, and decision-making processes involved in selecting optimal sensor positions to achieve specific objectives. For the purposes of this thesis, two of such techniques were considered, both presented below.

2.5.1. Optimal sensor placement

Optimal sensor placement involves a sensor placement architecture that incorporates various approaches to determine the most important strain features for measuring and the most strategic locations for placing sensors in a given structure. This architecture utilizes optimization theory, which is a mathematical framework that aims to find the best solution among a set of possible alternatives. The objective function for strain sensor placement depends on the specific goals and requirements of the monitoring application. Common objective functions include maximizing strain detection, achieving optimal strain distribution coverage and assessing structural integrity. By leveraging optimization theory and considering these objective functions, optimal sensor placement ensures that sensors are strategically positioned to capture critical data, enhance monitoring effectiveness, and facilitate informed decision-making for strain monitoring in metallic structures.

The primary hurdle faced by a sensor placement technique lies in its computational complexity, which varies greatly depending on the specific problem at hand. For instance, when aiming to optimize the selection of k sensors from a pool of n potential locations in order to maximize the objective function's value, a total of:

$$N_C = \binom{n}{k} = \frac{n!}{k!(n-k)!}$$

(14)

combinations must be taken into account. In essence, for each of thsese N_C combinations, the objective function needs to be computed. Ultimately, the combination of sensor locations that yields the highest value of the optimization function is considered to be the optimal architecture.

2.5.2. Engineering judgement

In many scientific problems, the number of combinations (N_C), to be considered is often too large to be computationally feasible. These problems pose challenges when attempting to exhaustively explore all possible combinations or solutions due to the prohibitive computational resources required. In such cases, decisions over the sensor placement architecture can be made by the judgment of the design engineers. In order to do that, a few things have to be understood about the desired sensor reading.

The ideal sensor reading would exhibit a 1-by-1 relationship between the measured strain ε and the quantity of interest Q being monitored. In an ideal scenario, this 1-by-1 relationship would hold across the entire range of values expected for the quantity of interest. However, in certain physical problems, achieving such ideal readings is not possible. Therefore, it becomes necessary to establish an evaluation method for sensor readings. The evaluation of sensor readings will be based on the following criteria, which will be defined and explained through an example involving a comparison of two different sensor readings:

❖ *Coverage*

The objective is to achieve an optimal coverage of the strain distribution across the structural area that is to be monitored. Placing sensors far from each other may result to blind spots, areas where monitoring is poor. In order for a reading to be trustworthy, it has to be a 1-by-1 function. The coverage of the sensor can be defined as the range of the quantity of interest for which the sensor's reading is a 1-by-1 function, as illustrated in Figure 12 for two different sensors, "A" and "B".
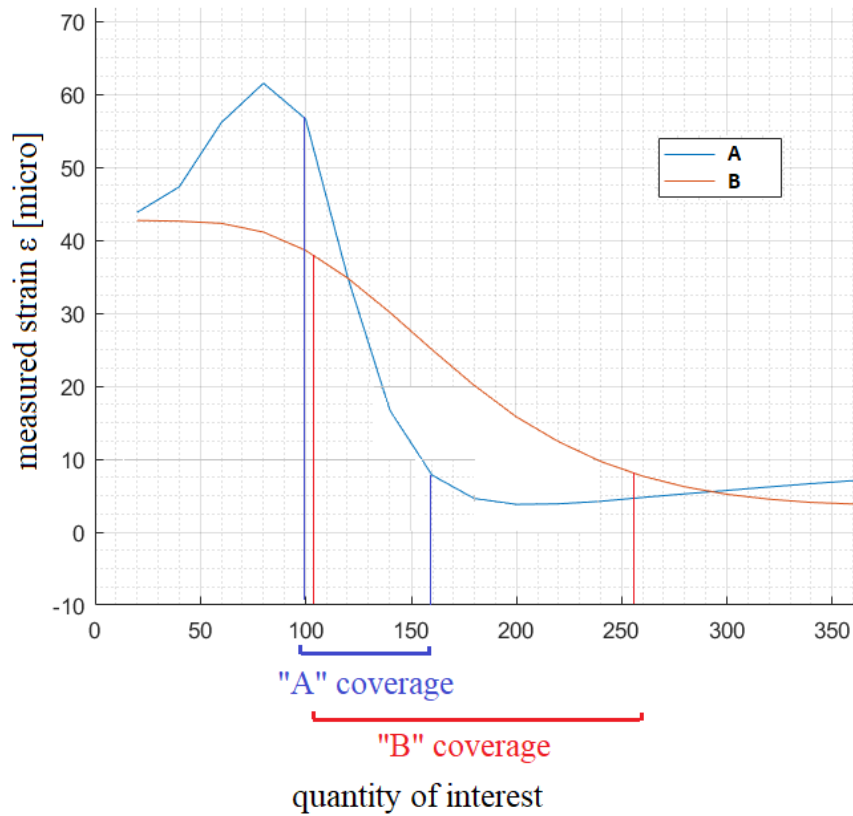
Figure 12: Definition of the coverage of sensor readings for two indicative sensors "A" and "B"

❖ *Accuracy*

The objective is to maximize the signal to noise ratio. This leads to more trustworthy readings because noise levels are considerably lower than the readings. Within the senso's coverage, its accuracy can be viewed as the steepness of the function $\left|\dfrac{dQ}{d\varepsilon}\right|$ as illustrated in Figure 13 for two different sensors. A higher value of $\left|\dfrac{dQ}{d\varepsilon}\right|$ indicates a greater sensitivity of the sensor, which in turn implies a higher accuracy of the measurements.
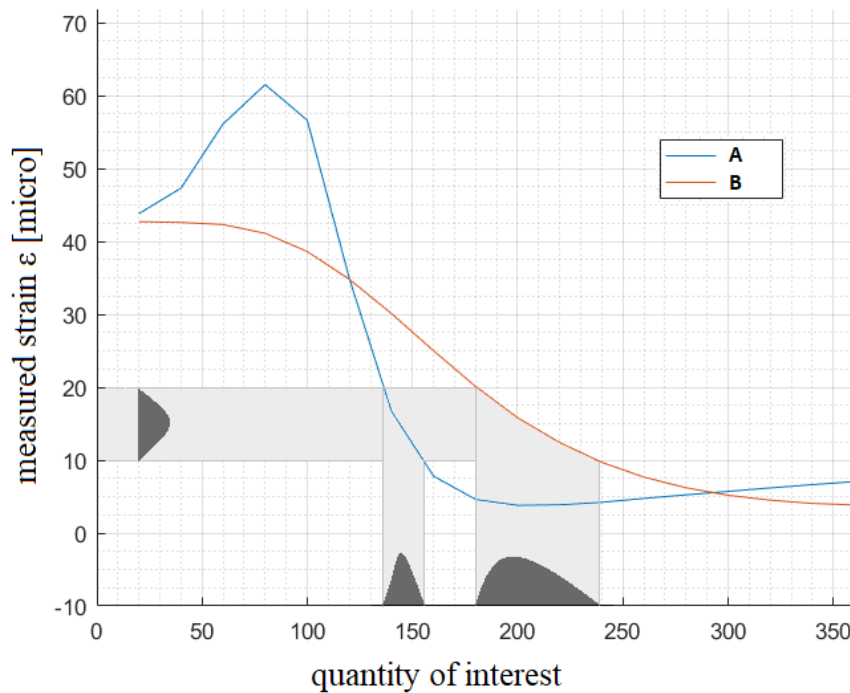
Figure 13: Definition of the accuracy of sensor readings for two indicative sensors "A" and "B"

Let us consider a strain reading with a 90% confidence interval laying between 10 and 20 με due to white noise effects as presented in Figure 13. Strain sensor placed in location "A" will translate this reading to a crack length 90% confidence interval ranging between 130mm to 150mm. In contrast, a strain sensor placed in location "B" will translate this reading to a crack length 90% confidence interval ranging between 180mm to 240mm. It is clear that sensor "A" has a higher accuracy than sensor "B", as the calculated crack length ranges only 20mm for sensor "A", but as much as 60mm for sensor "B". This is due to the fact that the $\left|\dfrac{dQ}{d\varepsilon}\right|$ is higher for sensor "A" than sensor "B".

However, strain sensor placed in location "A", which is noted with a blue color, doesn't give readings that are injective functions for crack lengths lower 110mm and higher than 150mm. So it cannot be used for detecting cracks with lengths beyond these limits, thus its coverage is [100,160]. In contrast, strain sensor placed in location "B" has a wider strain distribution coverage of [100,250]. So, strain sensor placed in location "A" may result in more accurate predictions than sensor "B", but it has a narrower crack length coverage. On the other hand, sensor "B" has a wider crack length coverage than sensor A but a lower accuracy. These criteria have to be taken into account when performing sensor placement.

❖ *Cost*

As stated in the introduction, the implementation of preventive maintenance in the form of crack growth SHM is deemed unappealing from a risk management perspective, considering the current utility functions used by the merchant shipping industry. There are two primary reasons why crack SHM is less attractive than simple crack repair: first the substantial cost associated with such a system and second the lack of support for such a policy by classification societies. The resolution of the second reason is contingent upon the resolution of the first, with cost being the most significant parameter.

The primary component influencing the cost is the selection of sensor types, such as Resistive Strain Gauges, Fiber Optic Sensors, Capacitive Sensors, and others. Additionally, the total number of sensors employed also impacts the overall cost, with a higher number of sensors resulting in increased expenses. However, it is worth noting that in some cases, such as Fiber Optic Sensors, the relationship between the number of sensors and cost may not follow a linear pattern. Sensor design engineers should take this into account during the planning and implementation stages to ensure cost efficiency. However, it is essential to emphasize that within the scope of this thesis, the evaluation of sensor placement only considers the criteria of coverage and accuracy.

3. Demonstrative case study

For this study a representative case of a cracked plate in a 7800 TEU VLCS is examined. The main particulars of the ship are presented in Table 2 while the midship section characteristics in Table 3 [39]. For the purposes of this work, it is considered that during a survey a through thickness crack has been identified on a longitudinal girder in the double bottom amidships at y = - 4010 mm on the starboard side. The girder plate has a thickness of $t = 20$ mm, a width of $W = 800$ mm and a length of $L = 1600$ mm while it extends between two frames. The crack is considered to have initiated from the weld toe of the longitudinal stiffener and propagated at the z direction as shown in Figure 14, while its longitudinal position is in the middle of the girder plate. An available measurement of the initial crack length is considered available and equal to 40 mm.

Table 2: Main particulars of 7800 TEU VLCS.

Name	Notation	Value	Units
Length Overall	L_{OA}	334	m
Length Between Perpendiculars	L_{BP}	319	m
Breath moulded	B	42.8	m
Depth to main deck	D	24.6	m
Draught scantling	T	14.5	m
Displacement full load	DWT	41,850	t
Block coefficient	C_B	0.67	-
Service Speed	V_S	25.4	kn
Engine power	MCR	69,620	kW

Table 3: Midship section characteristics of 7800 TEU VLCS.

Name	Notation	Value	Units
Moment of inertia of z axis	I_{zz}	670	m^4
z coordinate of neutral axis	z_{NA}	11.4	m
Detail of interest z coordinate	z	1.5	m
Material used in DB & lower box		AH32	
Material used in deck & upper box		AH36	
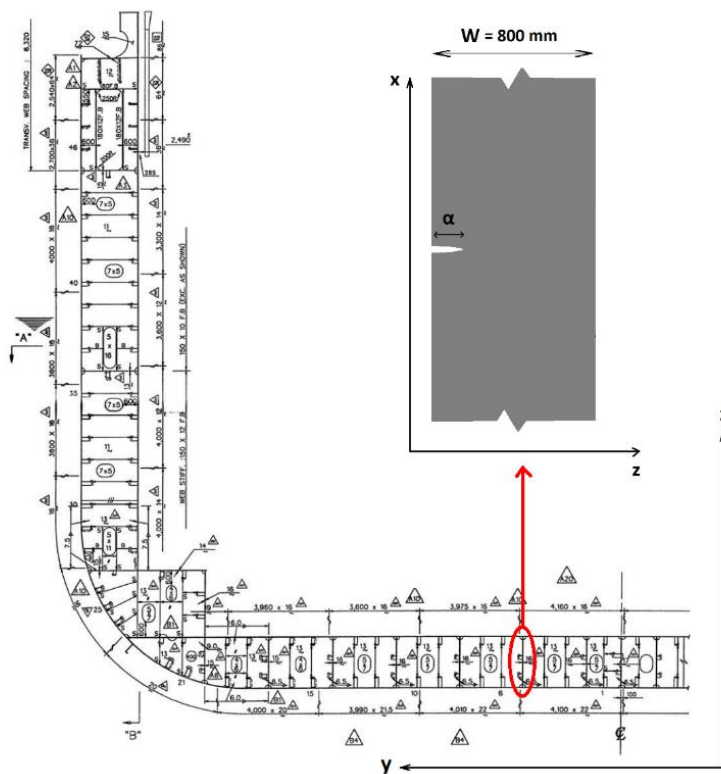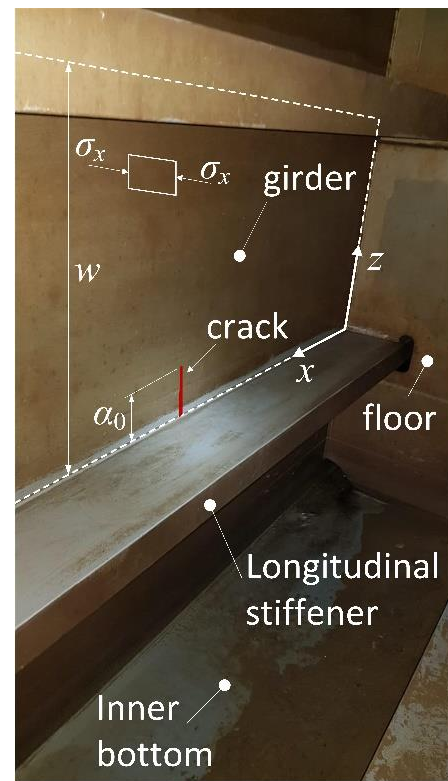
(a)   (b)

Figure 14: Midship section of 7800 TEU VLCS (a) and a picture indicating the crack location (b).

The cause of the flaw propagation is fatigue and corrosion fatigue. So, these will be the damage mechanism considered in the following analysis. Moreover, as the ship is under cathodic protection, the damage rate is assumed the same as if no corrosion took part, according to standards, thus only fatigue will be assessed in the following chapters.

The objective of this case study is twofold:

- To conduct a fatigue assessment utilizing the proposed method, which will also provide estimates for the physics-informed priors required for the Bayesian schemes.

- To develop a surrogate model of the cracked structural element by utilizing data generated from a Finite Element Method (FEM) model, which will also facilitate the estimation of the likelihood function for the Bayesian schemes.

3.1. Fatigue assessment

3.1.1. Fatigue load estimation

The choice of the ocean environment (e.g., North Atlantic) and the corresponding wave spectrum description (e.g., Pierson-Moskowitz, Brettschneider etc.) depends on the operational profile of the vessel at hand. The joint distribution of H_S and T_Z for this study was produced by utilizing data for the North Atlantic Ocean environment [15]. In detail, (H_S, T_Z) pairs were sampled using information from the North Atlantic Wave Scatter Diagram provided by ABS [9]. This was achieved by fitting the initial histogram using piecewise cubic Hermite interpolating polynomials (PCHIP) to obtain the empirical cumulative distribution function (eCDF), which was then employed to obtain the joint pdf illustrated in Figure 15. Implementing LHS, as described in Section 2.1, by utilizing this eCDF, the loading pairs $(H_S(i, j), T_Z(i, j))$ are sampled across all N sea states for all K crack growth paths.

The Bretschneider, also referred to as the two parameter Pierson-Moskowitz, wave spectrum is recommended for the North Atlantic [15] wave environment and was constructed for all $N \times K$ sea states in this through the following formula, using the loading pair $(H_S(i, j), T_Z(i, j))$ as a parameter:

$$S_\eta\left(\omega \,|\, H_S, T_Z\right) = \frac{H_S^2}{4\pi}\left(\frac{2\pi}{T_Z}\right)^4 \omega^{-5} \exp\left[-\frac{1}{\pi}\left(\frac{2\pi}{T_Z}\right)^4 \omega^4\right] \tag{15}$$
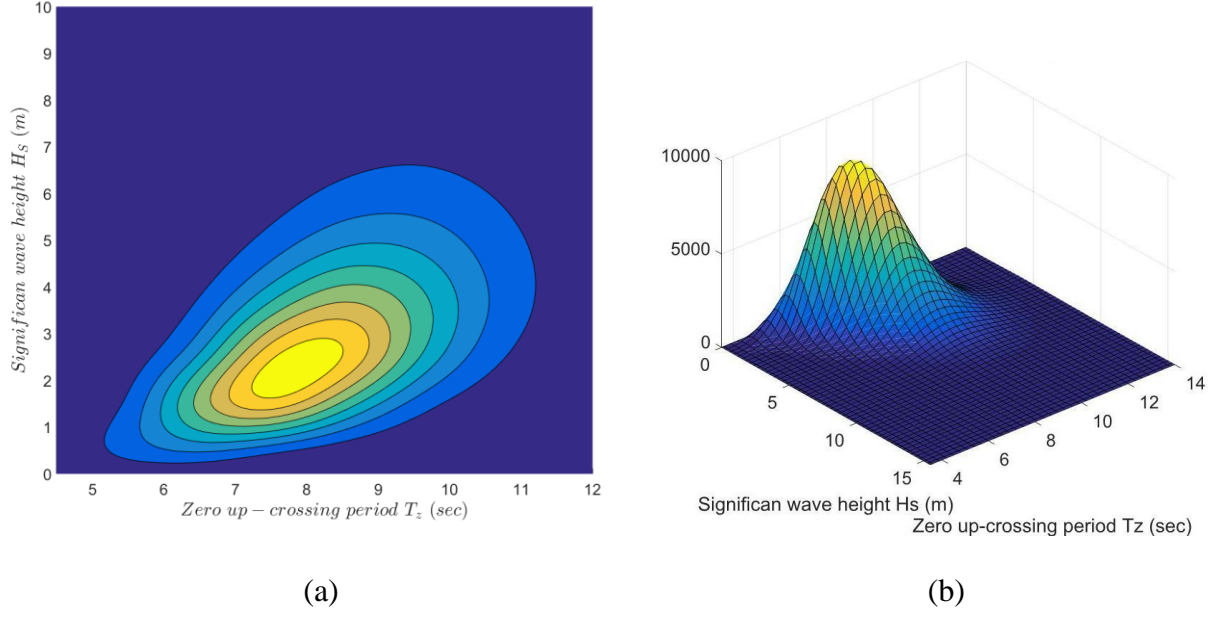
Figure 15: Contour plan of the empirical joint pdf of significant wave height H_S and zero up-crossing period T_Z as fitted from North Atlantic Wave Scatter Diagram as provided by ABS (a) and its fitted histogram (b).

The duration of a single sea state $\Delta\tau_{SS}$ was also treated as a random variable. In general, the duration of a stationary sea state ranges between 1-2 hours to 1-2 days, with mean values of 3-6 hours, for closed and open seas respectively [13]. So, for the North Atlantic Ocean, a sea state duration of around 6 hours can be considered as a reasonable assumption. Ultimately, it was assumed that the sea state duration $\Delta\tau_{SS}$ follows a uniform distribution ranging from 5-7 hours, resulting in a mean of 6 hours. The $\Delta\tau_{SS}$ was sampled across all $N \times K$ sea states utilizing Latin Hypercube Sampling (LHS).

In this study the derivation of the stress transfer function was done utilizing the wave induced vertical bending moment $RAO_{VBM}(\omega)$ of the 7800 TEU VLCS for fully loaded condition and zero heading angle. This was taken equal to the corresponding $RAO_{VBM}(\omega)$ of a similar 6250 TEU VLCS [40], thus assuming the two ships have the same hydrodynamic characteristics and weight distribution. For this case the loading condition LC and heading angle θ were assumed to be deterministic and constant through time. The structural detail assessed in this case is located near the bottom shell plating of the ship. It should be noted that in this study, secondary stresses were not considered, and only primary stresses were assumed. As the detail is close to the center plane of the ship, stresses due to the wave induced horizontal bending moment were assumed to be zero.

Ultimately, the stress transfer function at the detail of interest, which is illustrated in Figure 16, can be derived based on hull girder bending as follows:

$$H_\sigma(\omega) = \left|RAO_\sigma(\omega)\right| = \frac{z}{I_{ZZ}}\left|RAO_{VBM}(\omega)\right| \tag{16}$$
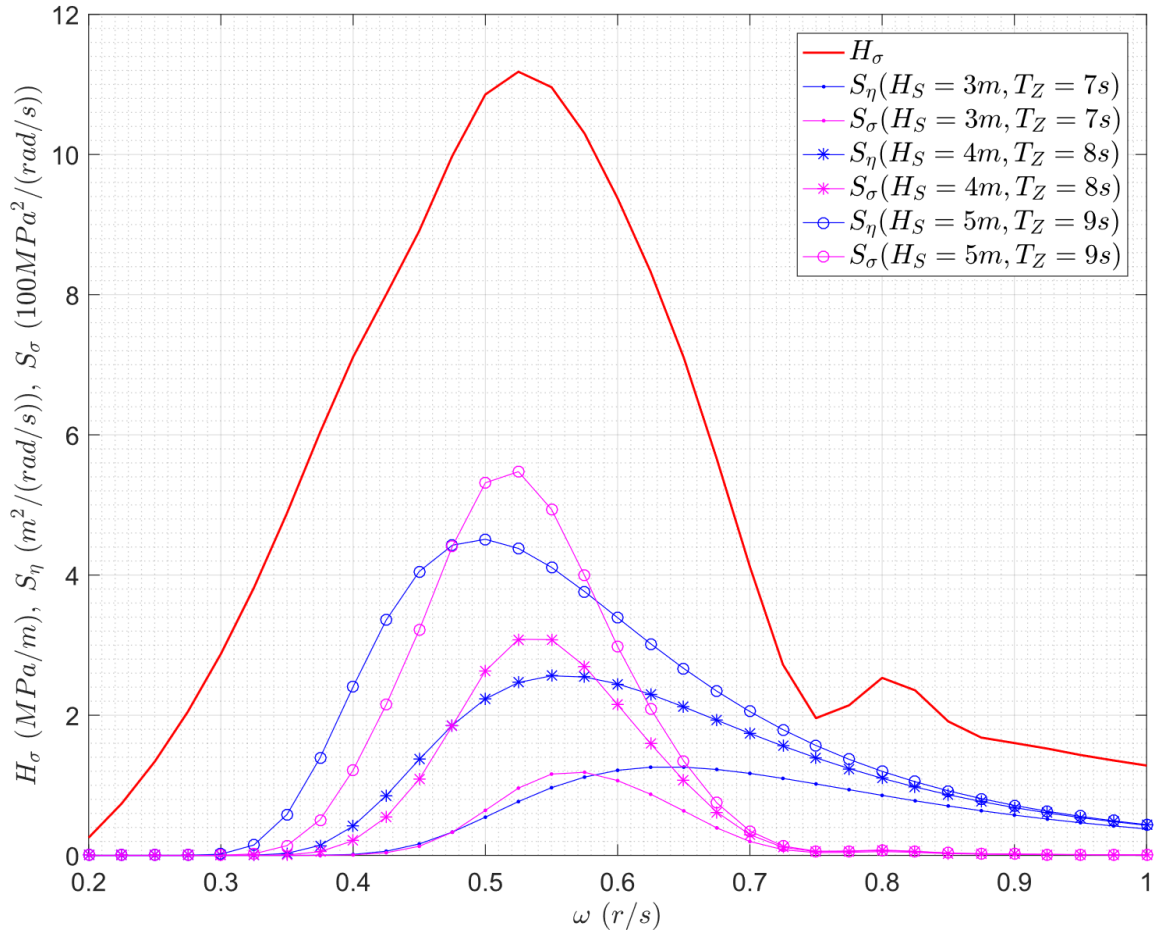
Figure 16: The stress and wave elevation transfer function for the point of interest (red), the wave spectrum (blue) and response spectrum (magenta) for three indicative sea states, given the ship is operating at service speed and heading seas.

The response spectrum and the fatigue loading pairs $S(i,j), N_{avg}(i,j)$ were calculated for all $N \times K$ sea states by the method presented in Section 2.1.2. The stress and wave elevation transfer function terms were obtained based on curves, such as those illustrated in Figure 16. So, the fatigue loading history matrix of the structure, which consists of the S, N_{avg} and τ arrays, can be sampled across all crack growth paths, in order to be utilized within the stochastic FCG model.

3.1.2. Crack growth model

In the present study, Paris-Erdogan law was used as the FCG model that describes the evolution of fatigue damage in time. Material parameters C, m and the initial crack size α_0 were treated as random variables following the distributions found in Table 4 and sampled across the different crack growth paths using LHS. During each sea state contained within each crack growth path, the material parameters $C(j)$, $m(j)$ and the fatigue loading pairs $S(i,j)$, $N_{\text{avg}}(i,j)$ are constants, thus Paris law can be analytically integrated within each sea state of each crack growth path:

$$\frac{d\alpha}{dN} = C \cdot \Delta K^m \Rightarrow \frac{d\alpha}{d\tau} = N_{\text{avg}} \cdot C \cdot \Delta K^m \ \ for \ \tau \in \left[\tau(i-1), \tau(i)\right] \tag{17}$$

$$\alpha(i+1,j) = \left(\alpha(i,j)^{-\frac{m(j)-2}{m(j)}} \cdot \frac{m(j)-2}{m(j)} \cdot C(j) \cdot Y^{m(j)} \cdot S(i,j)^{m(j)} \cdot \pi^{m(j)/2} \cdot N_{\text{avg}}(i,j) \cdot \Delta\tau_{\text{SS}}(i,j) \right)^{-\frac{2}{m(j)-2}} \tag{18}$$

where, the material parameters C and m were assumed to be correlated random variables and the recursive indices i and j refer to a particular sea state and crack growth trajectory respectively. The natural logarithm $\ln C$ follows a normal distribution with a mean $\overline{\ln C} = 29.84$ and a standard deviation of $\sigma(\ln C) = 0.55$ [5], corresponding to measurement units of $[\Delta K] = N/mm^{3/2}$ and $[d\alpha/dN] = mm/cycle$. According to the literature, a deterministic constant m has been often employed [5]. However, it has been shown that Paris law constants are probabilistic quantities that are highly correlated [41]. For that reason, the latter was assumed to follow a normal distribution with a mean of $\overline{m} = 3.1$ and a coefficient of variation $COV_m = 0.1$. Additionally, C and m were modeled so as to have a Pearson correlation coefficient of $PCC(C,m) = 0.9$. Nominally, these material parameters also depend on the loading condition in matters of both the applied stresses and the crack environment [5]. Namely, a high stress ratio $R = \Delta\sigma_{\max}/\Delta\sigma_{\min}$ results to a faster crack propagation, which can be quantified by corrections in the material parameters [19]. Knowledge over the structure's loading condition, may provide information on R and thus the constants C and m can be better approximated, although in this study it is assumed that ratio R is unknown, and mean values for C and m were taken [5].

In terms of the crack environment, cracks propagate with a faster pace when the tip is surrounded by corrosive environments. In detail, when the ship is in ballast condition, the crack is propagating under sea water environment which is corrosive, thus the crack growth rate is faster. In contrast, when the ship is fully loaded the crack propagates in air environment, and so a lower crack growth

rate is expected [5]. However, as the ship under study has a cathodic protection system installed, it is suggested that *C*, *m* values are to be taken the same as if the crack would propagate in air [5]. In case a vessel lacks cathodic protection, the loading condition can also be modeled as a variable that takes discrete values (0 for loaded and 1 for ballast condition) and included in the analysis. However, this was not pursued in the present study.

The minimum crack size that can be detected by an NDT is around $\alpha_0 \approx 10 \text{ mm}$, by focused phased array or by Zonal AUT [5]. So, crack assessment in general can only be applied for cracks equal to or greater than 10mm. The sizing error for NDTs is $\pm 7 mm$ while α_0 is often modeled as following a normal or lognormal distribution [5]. So, the initial crack size $\alpha(0, j)$ for this case study was assumed to follow a normal distribution with a mean equal to the measured crack size $\overline{\alpha_0} = 40 mm$ and a standard deviation of $\sigma(\alpha_0) = 2.3 \approx 7/3$ as listed in Table 4.

The geometry correction factor of a single edge crack of a plate is Y=1.12 for an infinite width plate. Since the crack induced stress field is not interrupted by the finite width of the plate, an assumption of an infinite width plate is reasonable. But this only occurs for small crack lengths. As the crack propagates this condition is violated. The geometry correction factor of a plate with a single edge crack is calculated for each crack length deterministically as [4]:

$$Y = 1.12 - 0.23 \frac{\alpha}{W} + 10.56 \left(\frac{\alpha}{W} \right)^2 - 21.74 \left(\frac{\alpha}{W} \right)^3 + 30.42 \left(\frac{\alpha}{W} \right)^4 \tag{19}$$

Table 4: Distributions of the model parameters.

Variable name	Not.	Units	Mean value	COV	PCC	Type	DIM
Geometry correction factor	Y	-	1.12	-	-	Deterministic	1×1
Material exponent	m	-	3.1	0.1	-0.9	Normal	$k \times 1$
Material parameter	C	-	1.3E-13	0.59		Lognormal	
Initial crack size	α_0	mm	20	0.05	-	Normal	$k \times 1$
Significant wave height	H_S	m	3.32	0.58	- 0.74	Empirical	$k \times n$
Sign. zero up-crossing period	T_Z	sec	8.46	0.19			
Sea state duration	$\Delta \tau_{SS}$	hours	6	0.10	-	Uniform	$k \times n$

3.1.3. Fracture Criteria

In order to calculate the $PoF(\tau)$, the distribution of the crack length $\alpha(\tau)$ at a given point in time is required. To achieve that, the crack is propagated using the FCG model for many sequential sea states until the crack length reaches a threshold value. Considering that the critical crack length α_{cr} is a random variable itself, which is calculated according to the C1 type criterion following the process described below, the crack length threshold is set such as to satisfy $CDF^{-1}(\alpha_{cr}) = 99.99\%$. At the time when α surpasses this value, it can be safely assumed that the crack propagation enters an unstable regime, where fracture may occur rapidly, as indicated by the crack lengths obtained by Paris' law tending towards infinity. The Fracture Assessment Diagram (FAD) is used for the assessment of the acceptability of a crack with length $\alpha(\tau)$ [5]. A general form of FAD is presented in Figure 17.
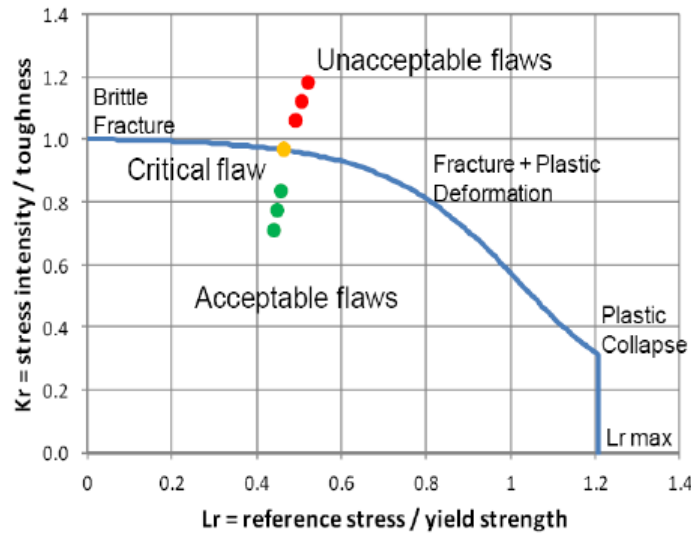
Figure 17: General form of a Fracture Assessment Diagram (figure adapted from [42])

According to the FAD, the load ratio L_{r} and the fracture ratio K_r are calculated as:

$$K_{\mathrm{r}} = \frac{K_{\max}}{K_{\mathrm{IC}}} = \frac{Y(\alpha) \cdot \sigma_{\max} \cdot \sqrt{\pi \alpha}}{K_{\mathrm{IC}}} , L_{\mathrm{r}} = \frac{\sigma_{\max}}{L_{\mathrm{r\,max}}} = \frac{\sigma_{\max}}{\dfrac{\sigma_{\mathrm{Y}} + \sigma_{\mathrm{U}}}{2}} \tag{20}$$

where K_{IC} refers to the fracture toughness of the material, $\sigma_{\max}$ refers to the maximum applied stress, α is the crack length, σ_{Y} refers to the yield stress and σ_{U} to the ultimate strength. As the crack is identified on a simple geometry, the following procedure, adopted from [5], is used for

the construction of the FAD. Namely, an assessment line is first defined according to the following formulas:

$$f(L_r) = \left(1 + \frac{1}{2}L_r^2\right)^{-1/2} \cdot \left(0.3 + 0.7 \cdot \exp\left(-\mu L_r^6\right)\right) \; for \, L_r \leq 1 \tag{21}$$

$$f(L_r) = f(1) \cdot L_r^{\left(\frac{N-1}{2N}\right)} \; for \; 1 \leq L_r \leq L_{r\,max} \tag{22}$$

$$f(L_r) = 0 \; for \; L_{r\,max} \leq L_r \tag{23}$$

where $\mu = \min(0.001 \cdot E / \sigma_Y, 0.6)$ and $N = 0.3 \cdot \left(1 - \sigma_Y / \sigma_U\right)$. According the employed procedure, a crack is considered acceptable only if the calculated assessment point (L_r, K_r) lies within the area bounded by the axes, the assessment line and the vertical line corresponding to L_r, K_r. Ultimately, the critical crack length α_{cr} for C1 was assumed to be equal to the crack length for which the crack was assessed to be unacceptable according to this procedure.

In order to determine the maximum tensile stress applied during the lifetime of the vessel at the detail of interest σ_{max}, the maximum bending moments corresponding to the case study vessel were used, as reported by Senjanović et al. [28]. Namely, these were equal to $VBM_S = 5.75\,\text{GNm}$ for sagging, i.e., vessel bottom in tension, and $VBM_H = -3.52\,\text{GNm}$ for hogging, i.e., vessel bottom in compression. As the crack studied is propagating under mode I, compressive stresses do not contribute to the phenomenon, thus it was assumed that only tensile loads lead to crack propagation. As the detail of interest is below the neutral y-axis of the cross-section of the ship, the maximum tensile stress applied in still water occurs during sagging, and therefore it follows that $\sigma_{max\,still} = VBM_S \cdot (z - z_{NA}) / I_{zz} = 85\text{MPa}$. In order to also consider the fatigue loading applied, conservatively a maximum applied wave induced tensile stress of $\sigma_{max\,wave} = \Delta\sigma_{max\,wave} / 2 = 25\text{MPa}$ was assumed. So, the maximum tensile stress applied can be calculated deterministically and was found to be:

$$\sigma_{max} = \sigma_{max\,still} + \sigma_{max\,wave} = 110\,\text{MPa} \tag{24}$$

Ultimately, the FAD was modeled probabilistically in order to obtain a critical crack length distribution. As such, the Youngs modulus E, yield strength σ_Y and ultimate strength σ_U were modeled as lognormally distributed random variables [14]. The mean values and coefficients of

variation (COV) for the above characteristics, corresponding to AH32 steel, were taken according to [14] and are presented in Table 5. No correlations were assumed between any of the model's random variables.

Table 5: Statistical structure of fracture assessment model (C1) parameters.

Variable name	Not	Units	Mean value	COV	Type	DIM
Fracture toughness	K_{IC}	MPa$\sqrt{m}$	180	0.28	Weibull $K_{min} = 20$MPa$\sqrt{m}$	$k \times 1$
Youngs modulus	E	GPa	210	0.05	Lognormal	$k \times 1$
Yield strength	σ_Y	MPa	315	0.07	Lognormal	$k \times 1$
Ultimate strength	σ_U	MPa	505	0.05	Lognormal	$k \times 1$

Fracture toughness K_{IC} is considered as one of the most uncertain parameters in defect assessment with available data for welded joints being exhibiting significant variability, especially for ferritic steels in the transition region [43]. In this work, it was assumed that the fracture toughness is defined by a three-parameter Weibull distribution with a shape factor of $k_{WBL} = 4$, a location factor $K_{min} = 20$MPa$\sqrt{m}$ for structural steel and only one remaining parameter to be determined from tests [5]. Assuming a mean $\overline{K_{IC}} = 180$MPa$\sqrt{m}$ is measured from A36 steel tests, the scale factor is calculated based on all above:

$$\theta_{WBL} = \frac{\overline{K_{IC}} - K_{min}}{\Gamma\left(1 + \dfrac{1}{k_{WBL}}\right)} = 176.5 \tag{25}$$

By performing forward uncertainty quantification by means of a MCS, different realizations of the critical crack length can be obtained through the process described by Eq. (21) - (26), resulting in the histogram of the critical crack length presented in Figure 18.
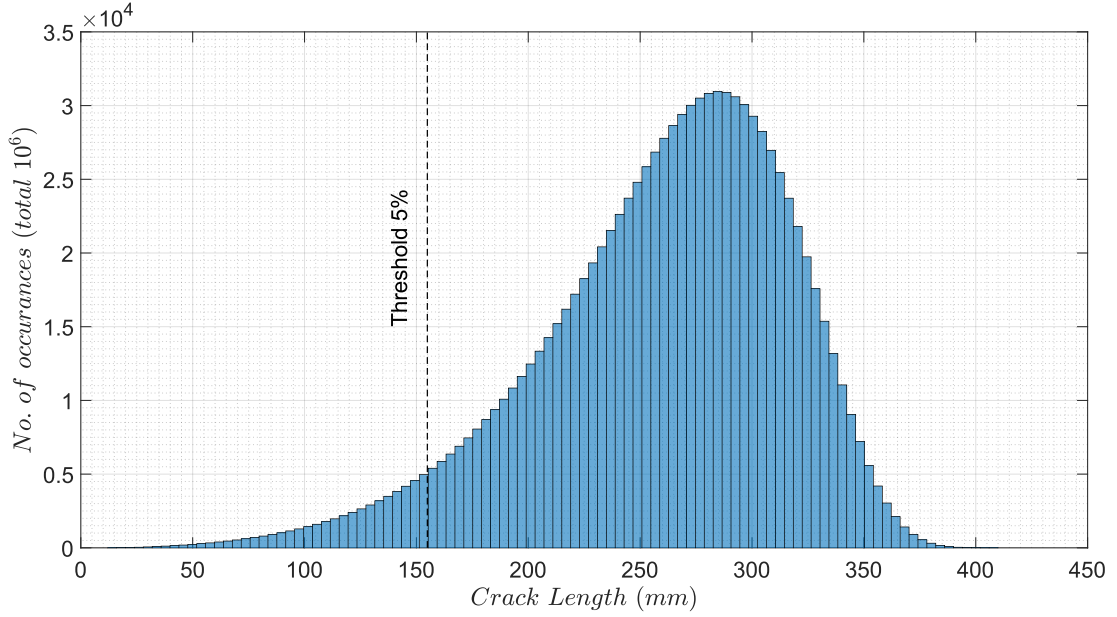
Figure 18: Distribution of the critical crack length $p(\alpha_{cr})$.

In order to calculate the probability of fracture under C1 at a given point of time τ, the distribution of α_{cr} was utilized. In order to calculate the RUL, critical crack length was assumed to take a set value corresponding to a 5% probability of non-exceedance based on this distribution, which led to an estimate of $\alpha_{cr5\%} = CDF^{-1}(\alpha_{cr}, 5\%) = 155\,\text{mm}$. The C1 criterion utilized operates under the assumption that the critical crack length α_{cr} is equivalent to the crack length for which the crack is assessed as unacceptable according to the aforementioned procedure. So, a higher threshold may as well be chosen depending on the risk tolerance of the ship's management.

The fundamental assumptions behind Paris law dictate that it holds for stress intensity factors ΔK that satisfy $\Delta K < \Delta K_{cr} \approx 40\text{MPa}\sqrt{\text{m}}$, while higher values result to unstable crack propagation. As there is clearly a limit to where Paris law can be utilized, an alternative criterion based on the crack growth rate, denoted as C2, is proposed herein. Namely, a critical crack growth rate is assumed to be equal to:

$$\left.\frac{\Delta\alpha}{\Delta\tau}\right|_{cr} = 7\,\text{mm/month} \tag{26}$$

The criterion is assessed by calculating $\Delta\alpha / \Delta\tau$ using a finite difference approximation for a given moment in time during the crack growth process and comparing it to the threshold value, upon exceedance of which failure is assumed to have occurred.

51

3.2. FEM model

The objective of this case study also includes the construction of a surrogate model that will have as inputs the crack length and as outputs the triaxial strain field across the plate's surface. In order to create such a surrogate model a finite element model of the cracked girder plate has to be created and solved, with the crack length as a parameter. Another possible input is the stress at the unaffected by the crack zone, which is the plate's external load S. However, the latter is left for future work and a far field stress of $P = 90$ MPa is assumed as seen in Figure 19.

The sides of the girder that are connected with the longitudinal stiffeners are considered to have a roller support that will only constrain the degree of freedom (DOF) of the z-direction displacement. Additionally, the sides of the plate connected to the floors are considered to be free of support. A fixed base point, meaning a single point that has all DOF constrained, and randomly chosen as seen in Figure 19. The structural problem to be solved in this case study is symmetric over the line parallel to the crack propagation line, that passes through the tip of the crack, as presented in Figure 19 (a). So, certain simplifications were made in order to simplify the setting and increase speed, as presented in Figure 19 (b). Specifically, symmetry constrains were applied solely to the non-cracked segment of the symmetry line, as seen in in Figure 19. Conversely, the cracked portion of that line was treated as a free edge, devoid of any external force interactions. This approach aligns with previous studies, such as the work conducted by [44] and [45], where a similar treatment was employed. By employing these simplifications, the computational complexity was reduced while maintaining the essential characteristics of the problem.
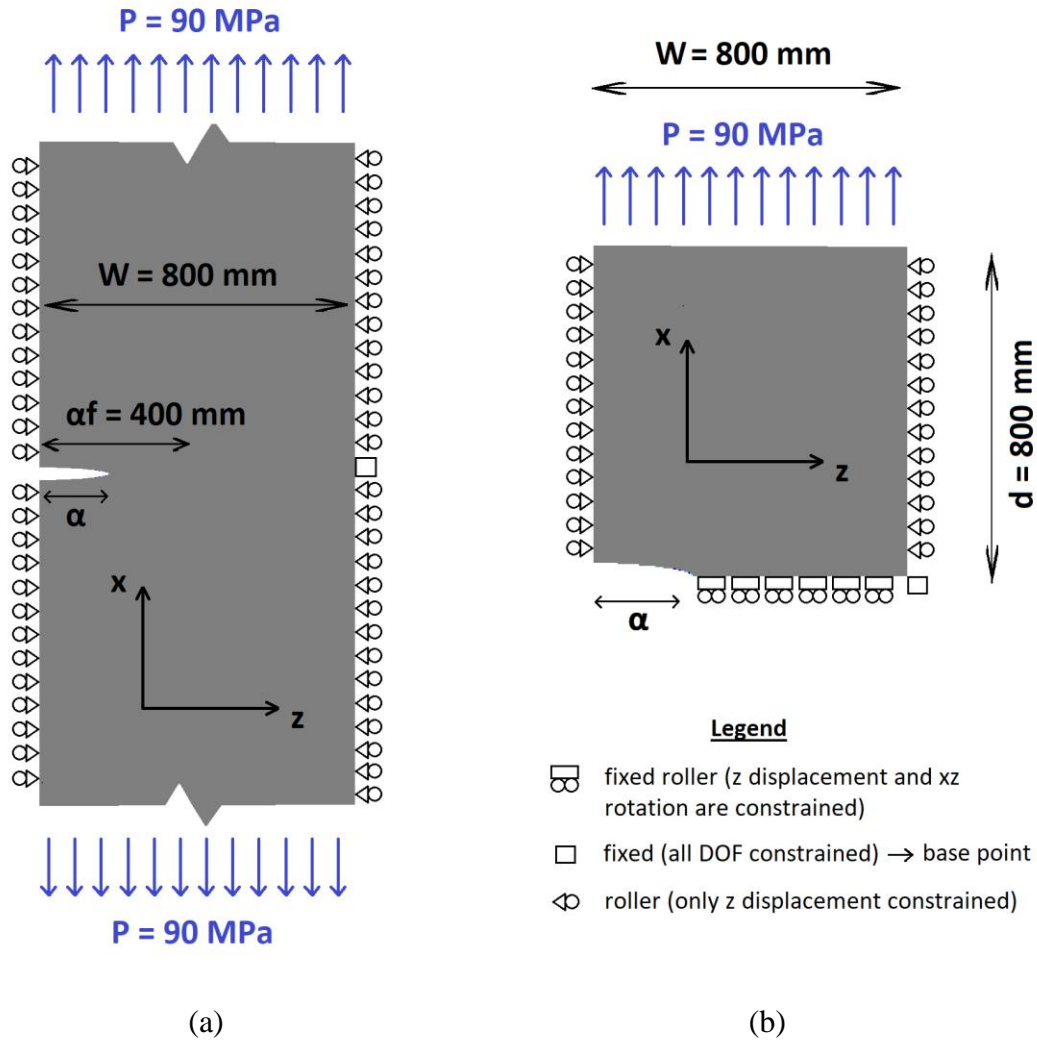
Figure 19: Cracked plate problem characteristics for the initial problem (a) and for the simplified problem due to symmetry (b).

The FEM model of the cracked girder plate was developed utilizing merchant Finite Element Analysis (FEA) software. The rest of this section outline the sequential steps undertaken to create and solve the FEM model of the cracked plate. First, the geometry of the cracked plate model, including its dimensions and crack length, are first specified. All points, lines and areas needed for creating the mesh are defined with the crack length as a parameter.

Despite the presence of a crack, the girder plate can still be considered a thin-walled structural element, exhibiting plain stress conditions far from the crack tip. While plain stress can be observed in the vicinity of the crack tip, the objective of this research is to investigate the behavior of the plate at a distance from the crack tip where sensors can be placed. Therefore, the problem

is treated as a plain stress problem, leading to the utilization of shell elements. Henceforth, the plate's thickness as $t = 20$ mm, is acknowledged as a section parameter. Specifically, in line with previous research [44], a four-node element with six degrees of freedom at each node was employed and adopted for this study as well. The plate material was assigned typical properties for steel, including a Young's modulus of $E = 210$ GPa and a Poisson's ratio of $v = 0.3$ [1].

The mesh density was increased gradually as it approached the crack region, which was achieved by defining points and lines in the geometry sector accordingly as illustrated for α=200mm in Figure 20. To account for the proximity to the crack tip, a larger number of nodes were selected for lines in close proximity to the crack. As the initial objectives necessitated the incorporation of the crack length as a parameter, enabling the definition of points and lines as functions of the crack length. The determination of such functions as long as the optimal number of nodes per line involved an iterative procedure of trial, evaluation, reassessment, and further adjustment.
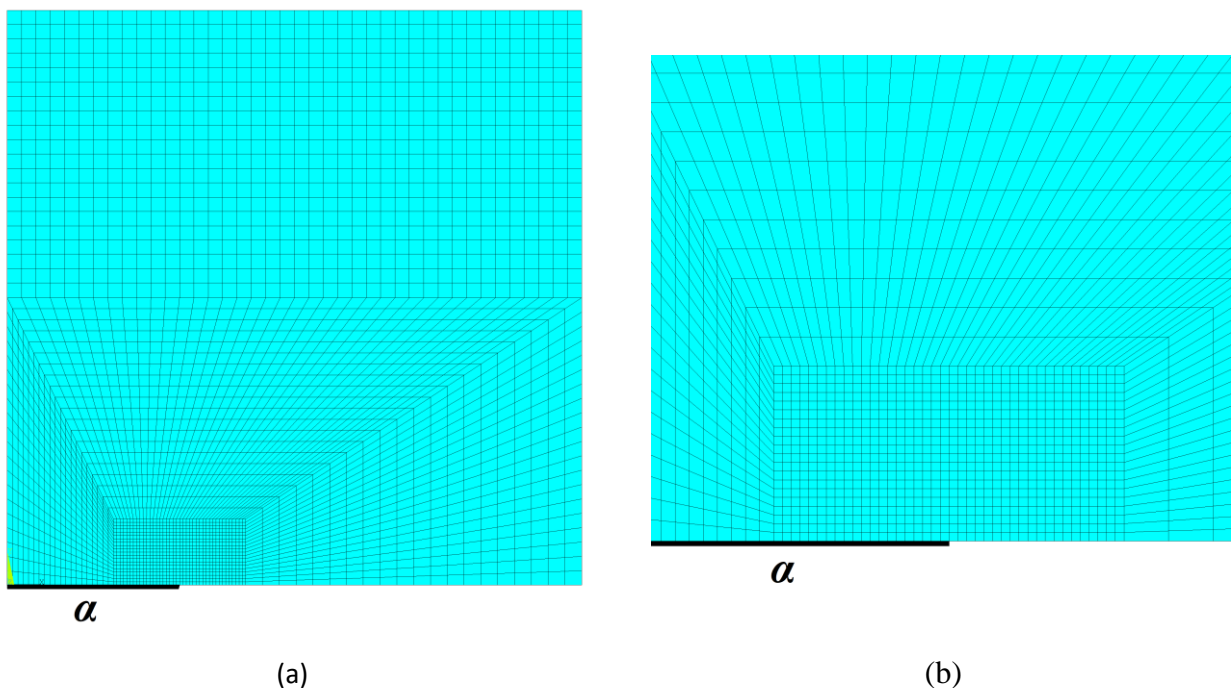

(a)   (b)

Figure 20: Meshing for crack length α=200mm (a) and its magnification close to the crack (b) in order to show the increased mesh density.

The literature commonly employs a meshing strategy to capture the behavior around the crack tip by gradually increasing mesh density as the tip is approached, a method also implemented in this study. This is typically accomplished by defining random or circular geometries and creating random [45], or circular element shapes [44] as depicted in Figure 21. In contrast, the present study adopts a rectangular meshing approach, resulting in finite elements with rectangular shapes.

While it is acknowledged that this choice may not represent the optimal solution, it is deemed adequate for fulfilling the specific objectives of this work. The appropriate boundary conditions, as described in the preceding paragraphs and depicted in Figure 19, were implemented in accordance with similar approaches found in the literature [45], as shown in Figure 21.
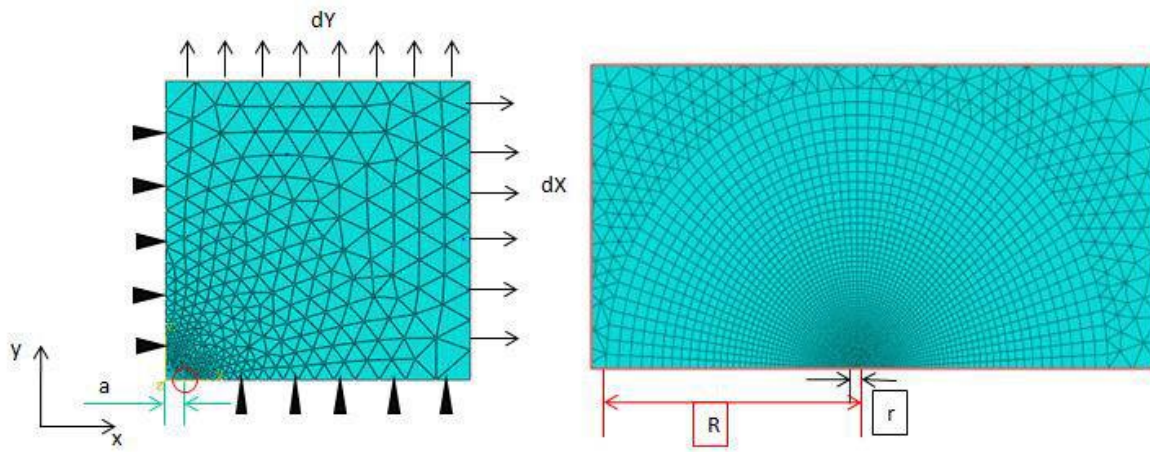

Figure 21: Meshing strategies of a cracked plate with random (a) and circular elements shapes (b)

Once the boundary conditions and loads are applied the model is solved. The results chosen to be extracted are the triaxial strain ($\varepsilon_z, \varepsilon_x, \varepsilon_{xz}$) for discretized points along certain z-directional paths, defined in Figure 22. This process was implemented for 40 crack lengths and 8 z-directional each discretized to 150 points, using a do-loop. Finally, the essential data for the generation of the surrogate model are gathered.
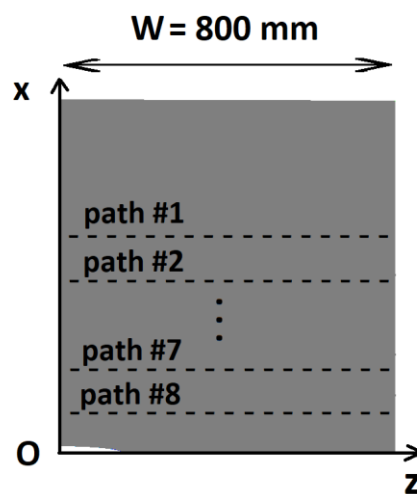

Figure 22: Paths in the z-direction where triaxial strain is obtained

3.3.Surrogate model

In the preceding section, an implementation of the FEM model was demonstrated. Nevertheless, the process of invoking and executing the merchant FEA software every time strain data is required proves to be impractical and time-consuming. To overcome this limitation, a surrogate model was developed. The key objective was to devise a function that accepts inputs such as the crack length (α), point coordinates (*x, z*), and the desired stress orientation, and provides the corresponding strain output at the specified point and orientation. This was achieved, by employing splines to interpolate the FEM generated data, effectively estimating the desired strain values based on the provided parameters. Since spline interpolation involves interpolating all data points without any fitting, the introduction of the Coefficient of Determination is unnecessary.

4. Results

In this chapter the results of the implementations described at the previous Section 3 concerning the case study, are presented and discussed. The chapter commences with the first part of the case study's objective, which is to assess the crack using the proposed method. Quantities of interest, such as the Remaining useful life (RUL) and the probability of fracture (POF) are presented alongside an assessment of the computational cost, convergence study, and method validation. Moreover, the first part concludes with a thoughtful discussion on potential avenues for future research. Moving on to the second part of the case study's objective, the outcomes of the Finite Element Method (FEM) model are showcased through strain fields observed on the surface of the cracked girder, accompanied by an assessment of computational cost. Furthermore, a Dimensional Analysis is conducted to inform the subsequent section, which entails a comprehensive discussion on sensor placement.

4.1. Fatigue assessment

A total of $K = 10^4$ crack growth paths, each one consisting of totally $N = 2 \cdot 10^3$ sea states was used for estimating the different QoIs for the case study employed herein. As a result of the time-discretization scheme employed by the proposed methodology (see Section 2.4) a non-smooth crack growth curve is obtained. The intersecting nature of the various crack growth paths is attributed to the random sequence of loading experienced by each path. These can be visualized in Figure 23 where a number of 15 indicative crack growth paths are presented. The fact that these individual crack growth trajectories intersect at various points, is not possible with either of the well-known methods discussed in Section 2.3. Within each sea state, i.e., each discretized temporal interval, the curves follow the exact Paris law shape.

Furthermore, it is evident that as time progresses, the variance of possible crack length values increases, indicating the increasing difficulty in predicting crack lengths further into the future, which aligns with intuitive expectations. Particularly, beyond a certain threshold specific to each crack growth path, the crack undergoes unstable propagation, serving as the anticipated trigger for the fracture criteria.
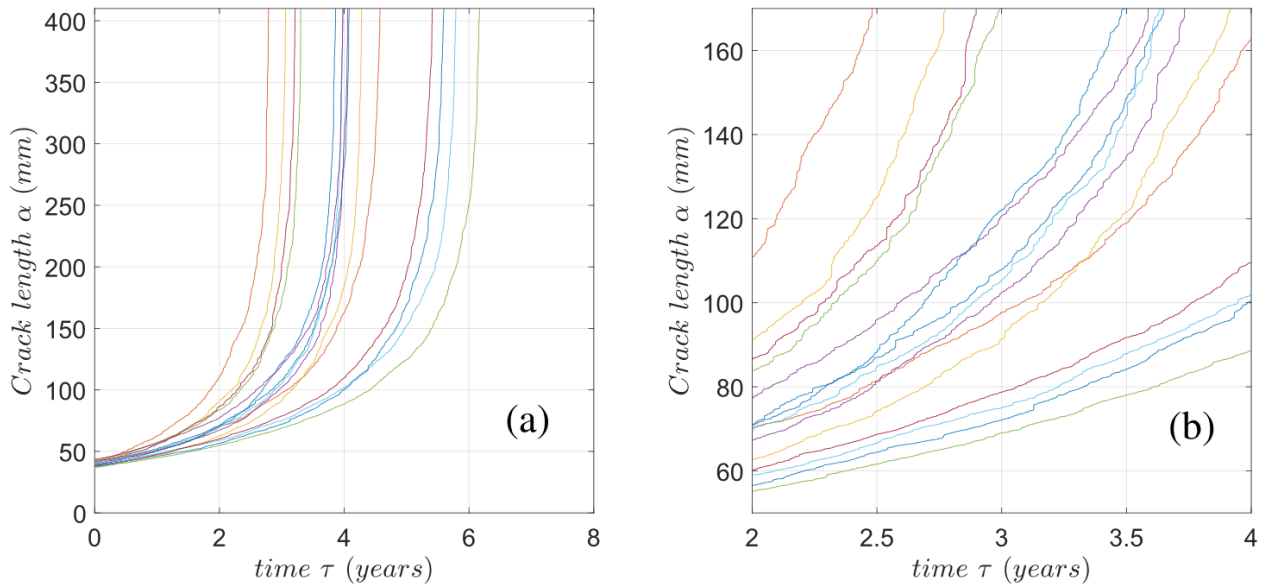
Figure 23: Indicative crack growth paths (a) and its magnification in a specific region (b) in order to show the intermingling provided by the proposed method.

4.1.1. Remaining useful life

As a result of utilizing C1, C2 or both criteria, each crack growth path corresponds to three values for the remaining useful life, denoted here as RUL_{C1}, RUL_{C2} and $RUL_{C1 \text{ and } C2}$ respectively. The total of $K = 10^4$ crack growth paths, ultimately result to three distributions of the RUL, which are presented in Figure 24 (a) over the entire lifecycle of the vessel. The criteria trigger points along with the crack growth paths are visualized in Figure 25. According to both criteria, a 5% non-exceedance probability translates to a remaining useful life of the structure around 2 years and 9 months, which is further shown in the detailed view in Figure 9 (b). As indicated by the results, C1 is satisfied for lower crack lengths than C2, thus leading a more conservative estimate of the remaining useful life, which can be further observed by the heavier tails of the C2-based RUL distribution shown in Figure 9 (a).
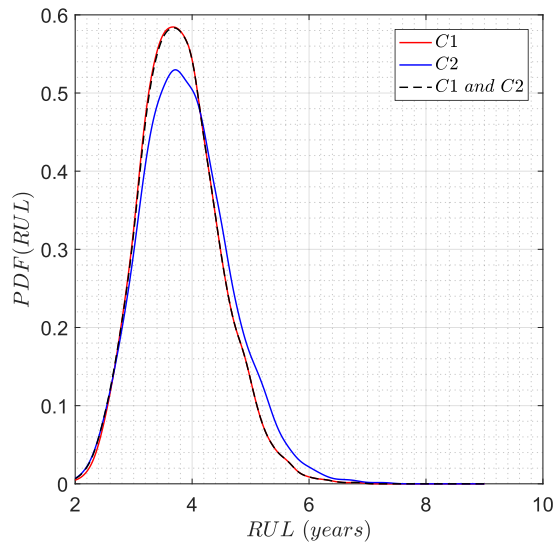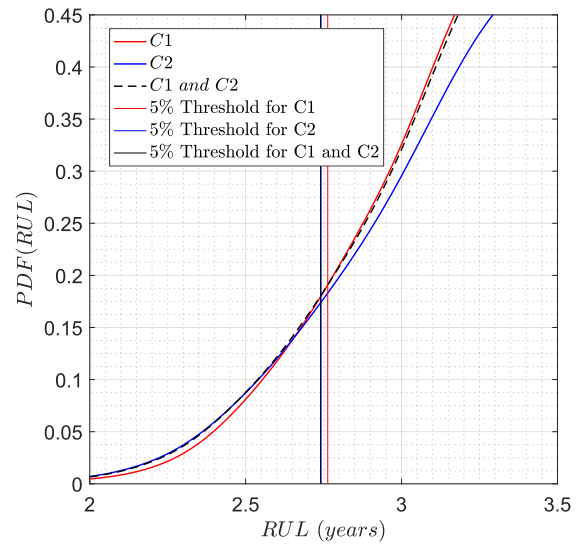
(a)   (b)

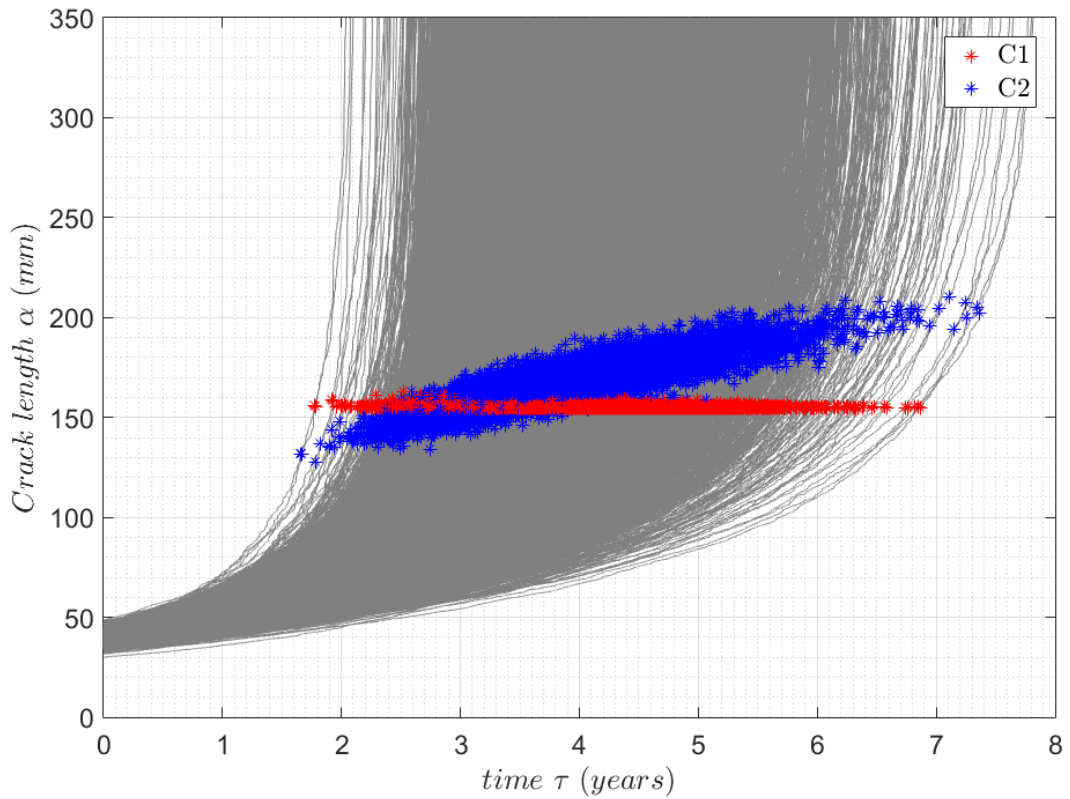Figure 24: Remaining Useful life density distribution (a) and cumulative distribution (b) utilizing C1 and C2 criterions.

Figure 25: C1 and C2 criterions satisfaction points on the crack paths.

4.1.2. Probability of fracture

At a given point in time each crack growth path corresponds to one realization of the crack length $\alpha(\tau)$. The total of $K = 10^4$ crack growth paths, result to a distribution of $\alpha(\tau)$, which is presented indicatively for $\tau=2,3,4$ years along with the critical crack length distribution as calculated solely by C1 in Figure 26. This resulted distribution of the crack length for a given point in time $\alpha(\tau)$, which is depicted as the orange histogram, constitutes the physics-informed prior function that can be utilized in Bayesian frameworks. For each point in time the $PoF(\tau)$ is calculated, by utilizing the above distributions and the method presented in Section 2.4 and is illustrated in Figure 27 (a). According to the method, the probability of fracture is expected to reach the value of 5%, 2 years and 11 months after the survey, which is indicated by the intersection of the dashed line with the $PoF(\tau)$ curve seen in the detail of Figure 27 (b).
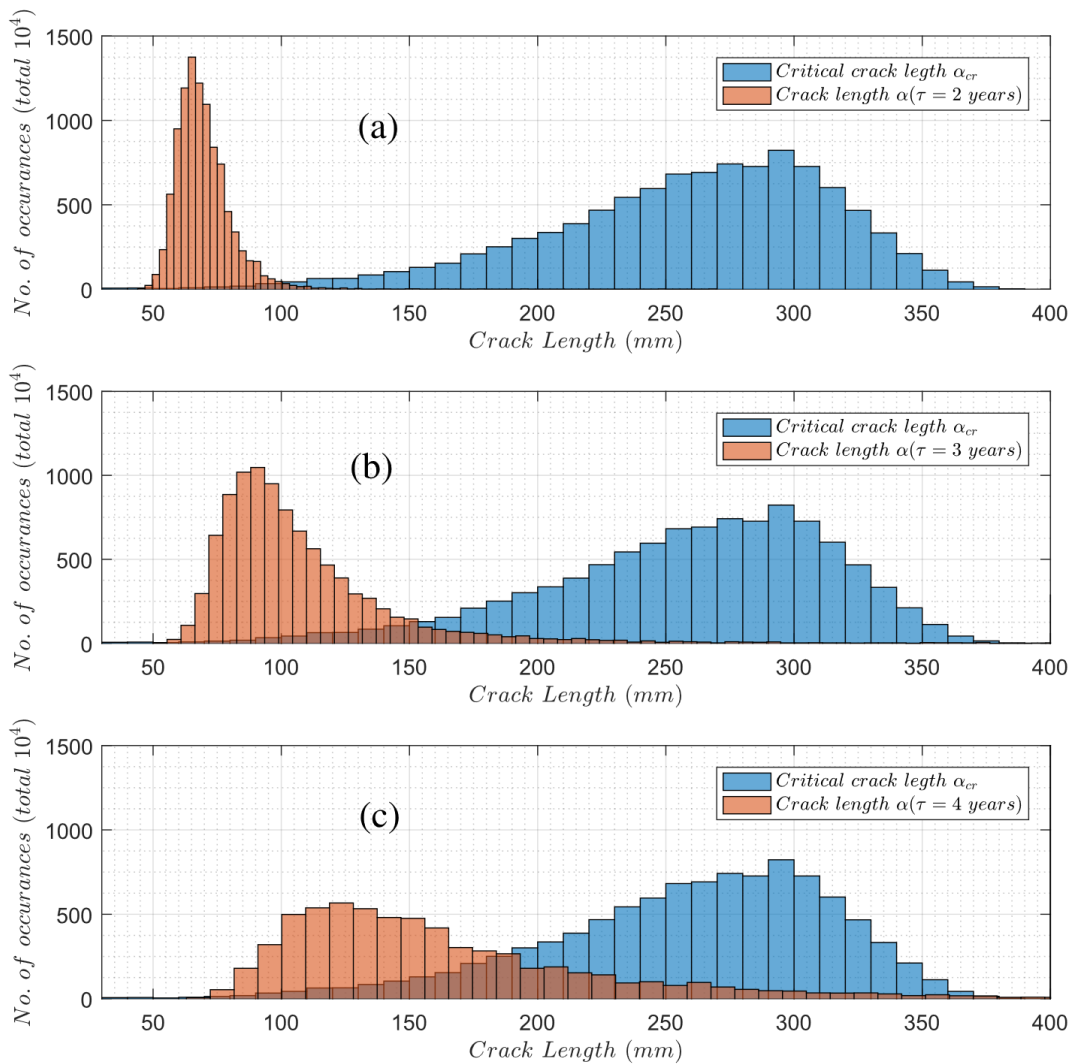
Figure 26: Distributions of α_{cr} and α for τ=2 years (a), τ=3 years (b), τ=4 years (c)
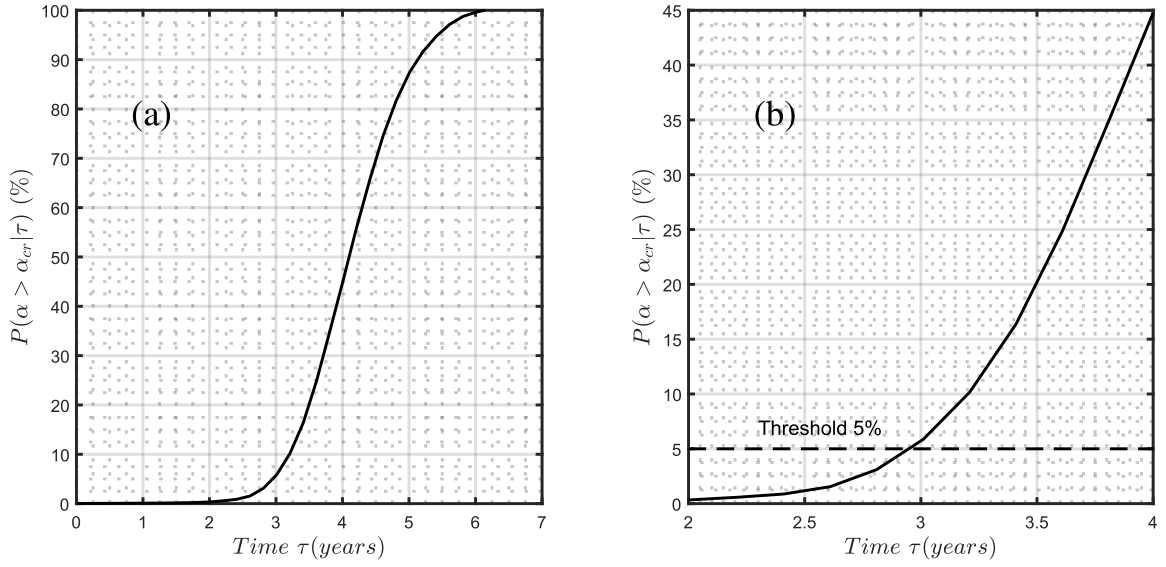

Figure 27: Probability of fracture over time $PoF(\tau)$ solely under C1 (a) and its magnification close to the point in time where threshold is reached (b).

4.1.3. Convergence study

In order to examine the convergence of the method, the authors resolved to apply it repeatedly over N_S runs with different sampling in terms of both *i* and *j* cases, that is the time discretization and number of samples in MCS of the FCG model parameters. A single individual run, which results to $K \times N$ cases, was used to calculate the mean and the standard deviation of $\tau(\alpha = 255mm)$ and $\alpha(\tau = 2.5\,years)$, noted as $\mu_{\tau|\alpha=255\text{mm}}$, $\sigma_{\tau|\alpha=255\text{mm}}$, $\mu_{\alpha|\tau=2.5\,\text{years}}$ and $\sigma_{\alpha|\tau=2.5\,\text{years}}$ respectively. In this convergence study, the above resulting statistics of one individual run correspond to one individual sample. Performing this run N_S times, a sampling size of N_S is gathered. The 99.7% confidence intervals of the gathered distributions of the means and standard deviations $\mu_{\tau|\alpha=255\text{mm}}$, $\sigma_{\tau|\alpha=255\text{mm}}$, $\mu_{\alpha|\tau=2.5\,\text{years}}$, $\sigma_{\alpha|\tau=2.5\,\text{years}}$ are presented in Figure 13 for different sampling sizes.
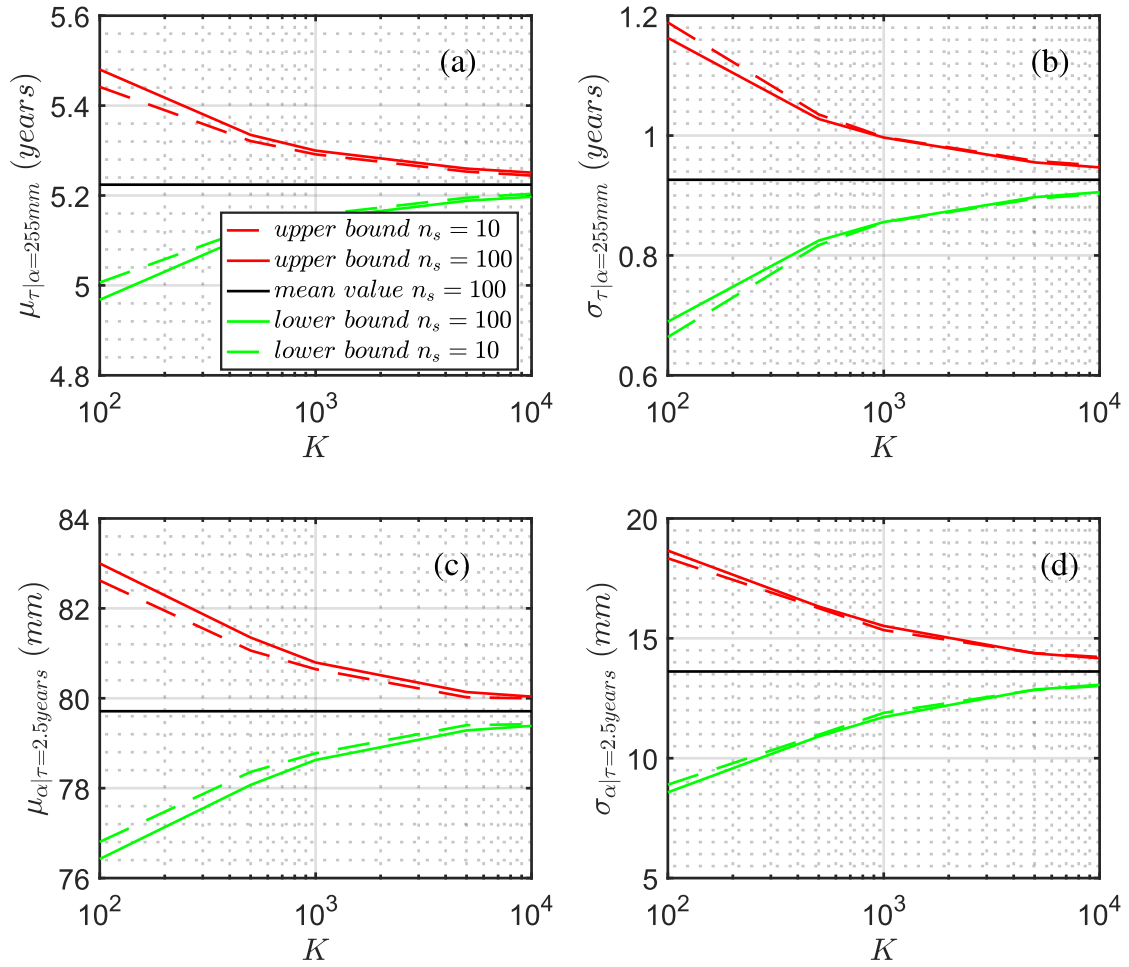
Figure 28: 99.7% confidence intervals of the gathered sampling distributions of $\mu_{\tau|\alpha=255\text{mm}}$ (a), $\sigma_{\tau|\alpha=255\text{mm}}$ (b), $\mu_{\alpha|\tau=2.5\,\text{years}}$ (c), $\sigma_{\alpha|\tau=2.5\,\text{years}}$ (d) for various crack growth paths sizes K and various sampling size N_S.

The confidence intervals of the chosen statistics are converging for a sampling size of $N_S = 100$ as there are no significant differences when compared to smaller sampling sizes. So, the 99.7% confidence intervals of the sampling distributions of $\mu_{\tau|\alpha=255\text{mm}}$, $\sigma_{\tau|\alpha=255\text{mm}}$, $\mu_{\alpha|\tau=2.5\,\text{years}}$, $\sigma_{\alpha|\tau=2.5\,\text{years}}$ are well approached. For $N_S = 100$, the coefficients of variation COV of the above distributions were calculated and presented in Figure 29. A COV less than 2% is considered acceptable, thus the method has a satisfying convergence for $K = 10^4$ as presented in Table 6.
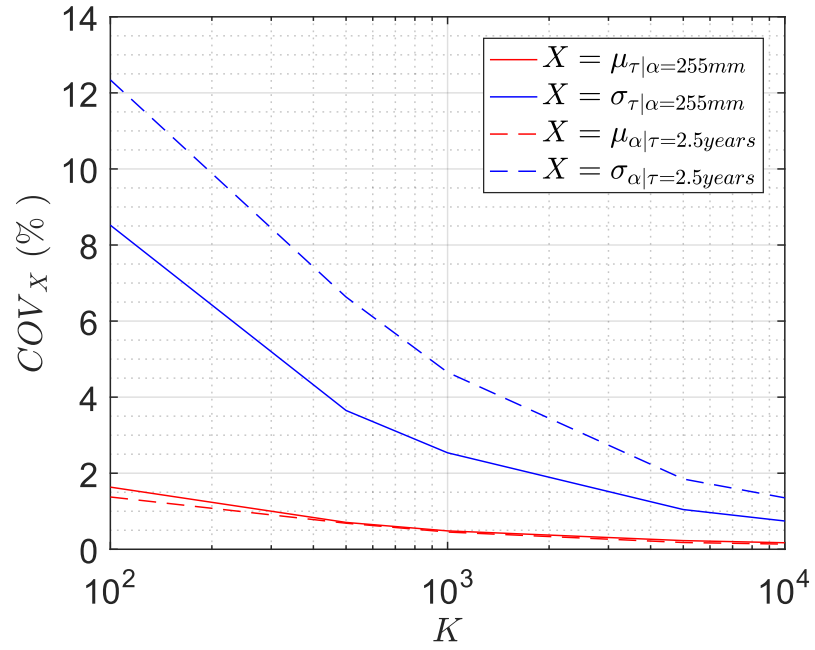
Figure 29: COV of the sampling distributions for various crack growth paths sizes K.

Table 6: COV of the sampling distributions for $N_{\mathrm{S}} = 100$ and $K = 10^4$.

Tested variable	COV for $K = 10^4$
$\mu_{\tau\|\alpha=255\,\mathrm{mm}}$	0.17%
$\sigma_{\tau\|\alpha=255\,\mathrm{mm}}$	0.74%
$\mu_{\alpha\|\tau=2.5\,\mathrm{years}}$	0.14%
$\sigma_{\alpha\|\tau=2.5\,\mathrm{years}}$	1.35%

4.1.4. Validation: comparing with CSR

The long-term distribution of the stress range that was calculated by the proposed was found to be close to the one proposed by the CSR. The proposed method led to the conclusion that a Weibull distribution defined by a mean value of 14.9 MPa and a shape factor $k = 1.6$ would constitute a reasonable approximation. On the other hand, CSR proposes a Weibull distribution defined by a shape factor $k \simeq 1$ plus another point $p(\Delta\sigma_{\mathrm{CSR}}) = 10^{-2}$ where $\Delta\sigma_{\mathrm{CSR}}$ is defined and calculated by CSR rules depending on the structure detail of interest, noted as hot spot area [6]. The comparison of those two distributions, assuming them having the same mean value, is depicted in Figure 30. It can be observed that the distribution obtained via the spectral analysis places most of its mass over a specific, relatively low stress range, which is reflective of the nature of the assumed wave environment (see Figure 5). Furthermore, a less heavy tail is observed, which implies smaller probabilities of occurrence for extreme events. This can also be justified based on the employed wave model, which is based on empirical data and naturally places higher probabilities on sea states that occur more frequently, compared to the rules-based distribution which could be tuned so as to account for rarer, but potentially catastrophic, events.
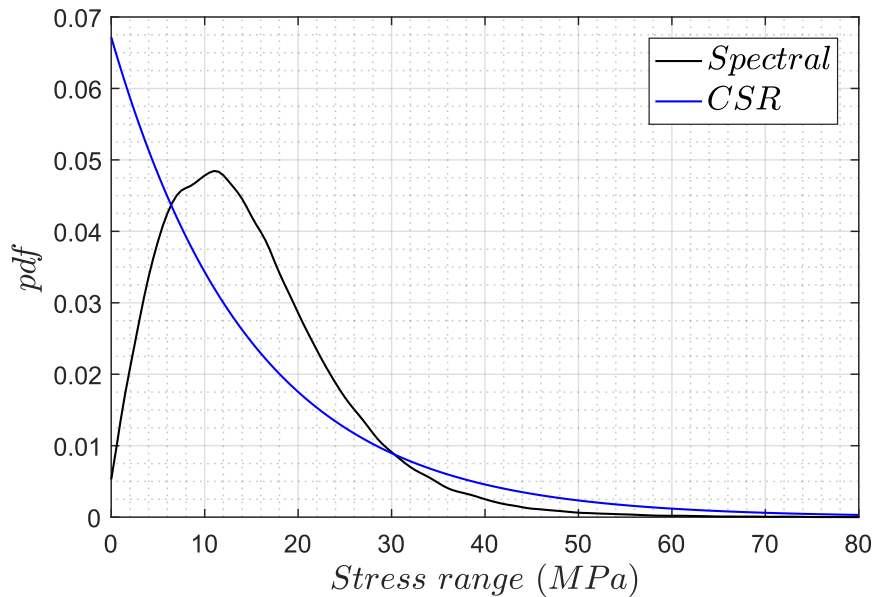

Figure 30: Long term stress range distributions according to CSR [6] (blue) and proposed method (black).

4.1.5. Computational cost

A comprehensive execution of $K = 10^4$ x $N = 2 \cdot 10^4$ cases Monte Carlo simulation, involving sampling and other processes, requires approximately 36 hours to complete. The significant computational expense is primarily attributed to the memory allocation technique employed by the MATLAB software. In this particular scenario, matrices of several gigabytes were allocated multiple times throughout the run. As a result, the wave scatter diagram sampling and the S, N_{avg} sampling were carried out independently from the main crack growth state model run. The latter task typically requires around 1 hour to reach completion.

4.1.6. Discussion

❖ *the REFAS system*

The construction of local structural models for all hot spot areas is the final step in developing a system-level fatigue assessment technique, following the global structural and hydrodynamic model. These local models allow for the calculation of quantities of interest (QoI) over time for both intact and cracked structural elements of the ship. Additionally, such a technique can be illustrated as a real-time fatigue assessment system, namely REFAS, which can have as input the actual operational fatigue load characteristics of the ship, as illustrated in Figure 31.

To achieve this, a digital twin methodology can be employed, incorporating the ship's structural and hydrodynamic models along with real-time wave data. The system-level fatigue assessment technique utilizes these inputs to generate the desired QoI. Real-time GPS signals provide information about the ship's location, speed, and direction (ψ). By exchanging location data with a meteorological website, real-time sea state statistics such as significant wave height (H), wave period (T), and wave direction (φ) can be obtained. The ship's direction and wave direction can be utilized to approximate the heading angle (θ). This information significantly reduces uncertainty regarding the marine environment, leaving mainly high uncertainty associated with material parameters.

For a more accurate approximation of the marine environment, a costlier alternative to GPS input is the installation of a "wave radar" onboard. This radar can directly measure real-time wave height (H) and frequency (ω), allowing for more precise long-term or even short-term representation of the marine environment. Consequently, the real-time wave data serves as an input to the system-level version of the proposed method, enabling the estimation of the real-time stress range at all hot spot areas and mapping the desired QoI across these areas.
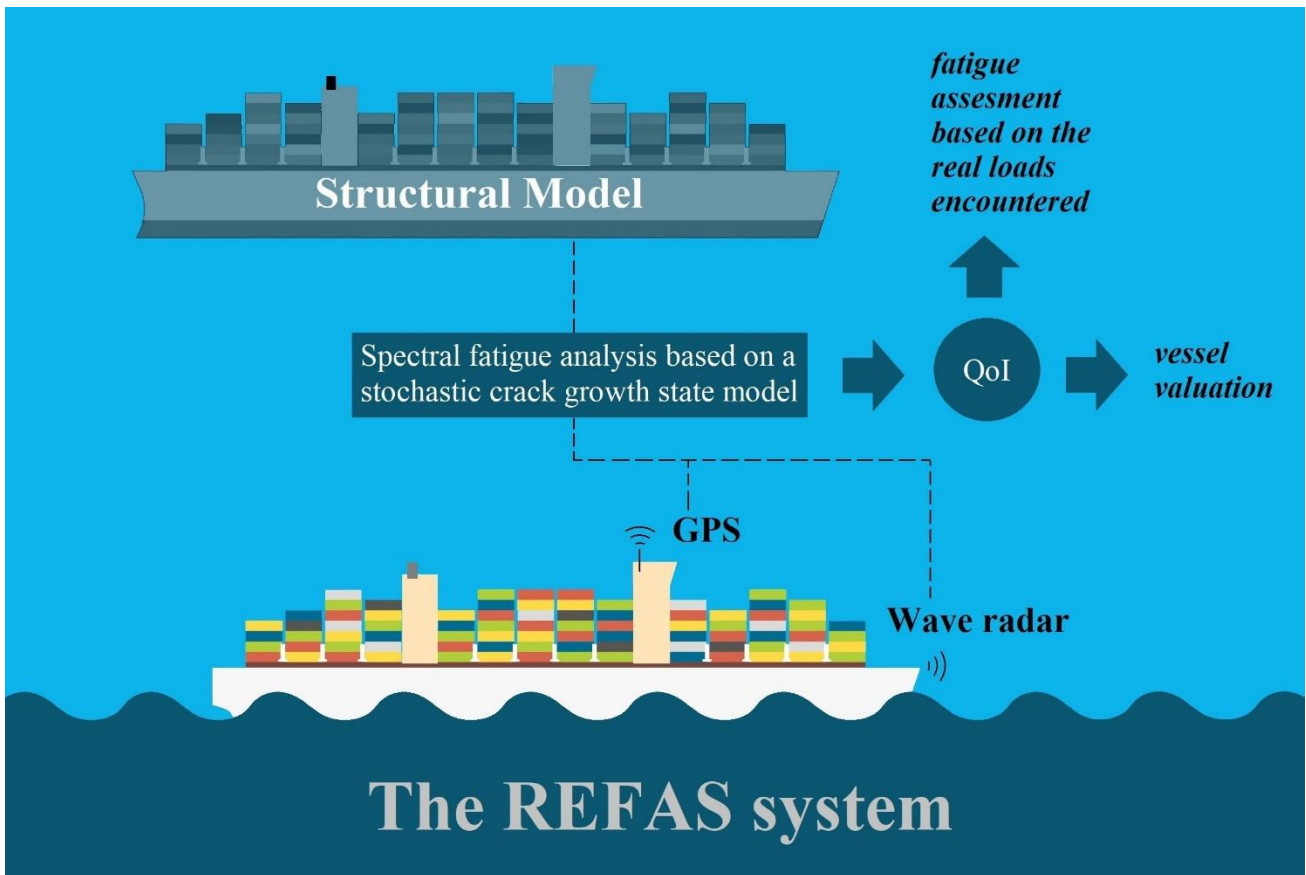
Figure 31: Representation of a real-time fatigue assessment system REFAS

The QoI obtained from a REFAS system has a direct impact on the resale price of a structure. The market's valuation of a second-hand ship can be supported by the QoI generated by a REFAS system. For instance, let's consider two sister vessels, referred to as "Vessel A" and "Vessel B," both constructed in the same year. Over a period of ten years, "Vessel A" predominantly operates in the North Atlantic, while "Vessel B" operates mainly along the maritime Silk Road. During this time, "Vessel A" is likely to encounter harsher sea conditions compared to "Vessel B," potentially leading to a shorter remaining useful life in terms of fatigue. Consequently, plastic deformations may be detected in "Vessel A" which can be considered in the market price of the asset. By installing a REFAS system in both vessels throughout this ten-year period, the structural disparities between them can be quantified, specifically in terms of fatigue, at a negligible cost. This quantification of their structural health condition can then be taken into consideration when determining the valuation of the vessels.

❖ *Short-term analysis*

In this study, the observed loading pair $S(i, j)$, $N_{avg}(i, j)$ conforms to a Rayleigh distribution within a specific sea state. Our proposed method assumes that the loading pair remains constant throughout the sea state and determines these constant values by utilizing moments of the stress response spectrum. This approach is widely adopted in the literature [15]. To improve the approximation of this assumption, it suggested to treat the short-term statistics in a similar manner as the long-term statistics employed by the proposed method. In other words, the duration of a sea state can be further divided into smaller intervals using an appropriate time discretization technique. During each interval, the observed stress range will be sampled from the Rayleigh distribution, while the loading frequency will be deterministic. The short-term equivalent constant stress range refers to the stress range that, if applied continuously for the entire duration of a sea state, would result in the same level of damage as that calculated by further subdividing time. To determine the short-term equivalent constant stress range, we will calculate it parametrically for various characteristics of the sea state. Subsequently, this value can be utilized within the long-term method, enhancing its accuracy and reliability.

4.2. Structural model

The FEM model of the cracked plate was established and solved for various crack length cases, as detailed in Section 3.2. Strain fields corresponding to the three components of stress, namely the x-directional strain ε_x, the z-directional strain ε_z and the xz-plane shear strain ε_{xz} were obtained for all the above cases. Contour plots illustrating the aforementioned fields ε_x, ε_z, and ε_{xz} are presented in Figure 32, Figure 33 and Figure 34 respectively, showcasing results for selected indicative crack lengths. To enhance visibility, a scale of 1:90 was applied to the displacements of all element's nodes, allowing the crack to be clearly observed by the reader.
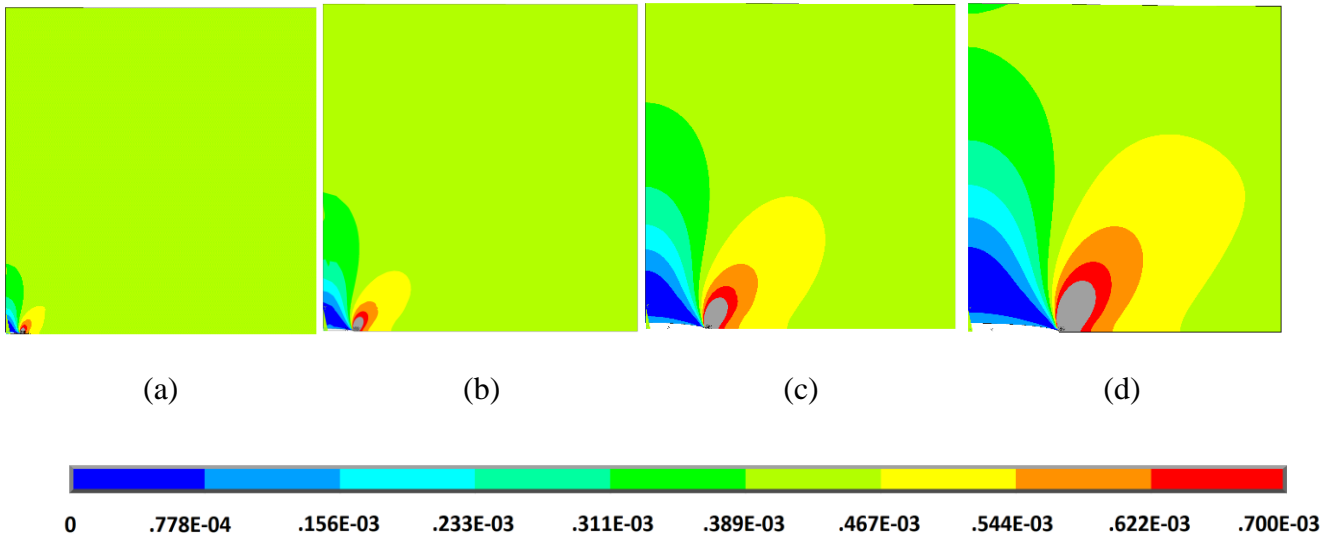
| | | | |
| (a) | (b) | (c) | (d) |

| 0 | .778E-04 | .156E-03 | .233E-03 | .311E-03 | .389E-03 | .467E-03 | .544E-03 | .622E-03 | .700E-03 |

Figure 32: x-directional strain ε_x fields for $\alpha = 40$mm (a), $\alpha = 80$mm (b), $\alpha = 160$mm (c) and $\alpha = 240$mm (d)

Upon observing the x-directional strain field ε_x in Figure 32, three distinct zones can be identified:

- the unaffected zone,
- the low-strain zone, and
- the high-strain zone.

The unaffected zone encompasses areas where the presence of the crack has minimal impact on the strain field. The material within this zone exhibit strains equivalent to those induced by the external force P, if applied to an uncracked plate $\varepsilon_{x\infty} = \dfrac{P}{E} = \dfrac{90\text{MPa}}{210\text{GPa}} = 429\mu\varepsilon$. This results in a green color representation in Figure 32. The low-strain zone extends along the regions surrounding the crack's free edge. In this zone, the material does not contribute to the plate's strength, and thus the induced stress and strain are zero. This zone is denoted mainly by the blue color in Figure 28. The high-strain zone extends around the crack tip and in the direction of crack propagation. Due to the failure of the low-strain zone to bear the load, stress concentrations occur, resulting in localized regions of significantly high strain. These regions are indicated by the grey and red colors in Figure 32.
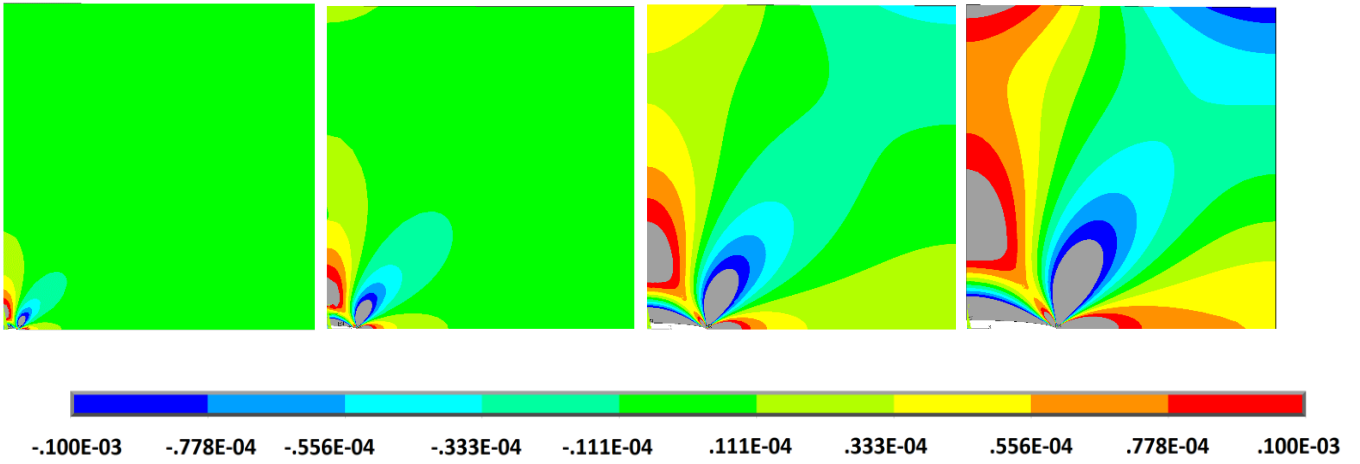
-.100E-03   -.778E-04   -.556E-04   -.333E-04   -.111E-04   .111E-04   .333E-04   .556E-04   .778E-04   .100E-03

Figure 33: z-directional strain ε_z fields for $\alpha = 40$mm (a), $\alpha = 80$mm (b), $\alpha = 160$mm (c) and $\alpha = 240$mm (d)

The z-directional ε_z and xz in-plane shear ε_{xz} strain fields can be treated similarly to ε_x. The unaffected zone can be defined for these fields again as areas where the presence of the crack has minimal impact on the strain field. The material within this zone exhibit strains equivalent to those induced by the external force *P*, if applied to an uncracked plate. However, in these cases, the value of $\varepsilon_{z\infty}$ and $\varepsilon_{xz\infty}$ is zero, as the external load is applied in the z-direction and does not induce strains in the z-direction or the xz-plane shear direction.

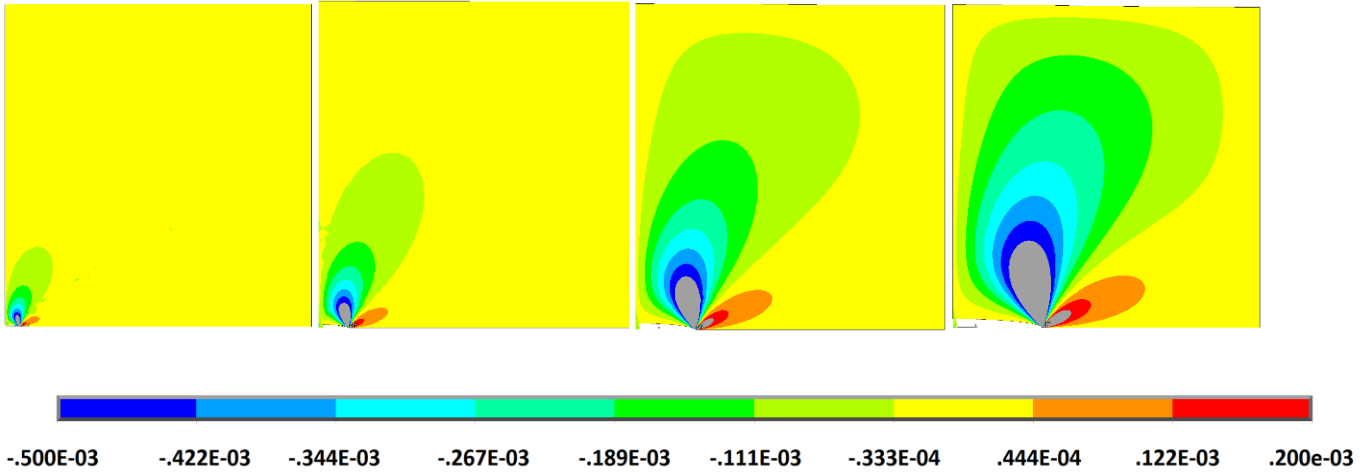-.500E-03   -.422E-03   -.344E-03   -.267E-03   -.189E-03   -.111E-03   -.333E-04   .444E-04   .122E-03   .200e-03

Figure 34: xz-plane shear strain ε_{xz} fields for $\alpha = 40$mm (a), $\alpha = 80$mm (b), $\alpha = 160$mm (c) and $\alpha = 240$mm (d)

4.2.1. Computational cost

The FEM model of the cracked girder plate was developed utilizing the ANSYS APDL. The creation and solution of the FEM model involved multiple crack lengths and were performed using the BATCH option available in ANSYS APDL. The ANSYS batch code, designed as described in Section 3.2, was executed for a total of 40 cases with varying crack lengths, resulting in an approximate runtime of 2 hours and 6 minutes. These cases encompassed crack lengths ranging from 40mm to 400mm, indicating that each individual Finite Element Method (FEM) model took approximately 3.5 minutes to complete the algorithm. Utilizing the outcomes of this run, a surrogate model was constructed using the MATLAB software, which significantly expedites the process. To reproduce the original data that required approximately 2 hours using the ANSYS batch code, executing the surrogate model takes approximately 7 minutes.

4.2.2. Dimensional analysis

For academic purposes, the width and length of the cracked plate are considered infinite in this paragraph, even if they are not considered as in the rest of this thesis. Considering the same problem as before but with this minor addition, the objectives are to relate the strain readings from place to place, in order to have a better understanding of the physical problem. The strain value ε_k, which is denoted as the dependent quantity, depends solely on the independent set of the following quantities: crack length (α), sensor location (x, z), stress load linear density (P), plate thickness (t), Youngs modulus (E) and the Poisson ratio (v).

$$\varepsilon_k = f(\alpha, x, z, P, t, E, v) \tag{27}$$

In the System International (SI), the dimensions of the dependent and independent quantities are:

$$\begin{cases} [\varepsilon_k] = [v] = 1 \\ [a] = [x] = [z] = 1\text{m} \\ [E] = 1\text{N/m}^2 \\ [P] = 1\text{N/m} \end{cases} \tag{28}$$

Inspection of the above shows that the three quantities α, E and P, for example, comprise a complete, dimensionally independent subset of the seven independent variables. The dimension of any one of these three cannot be made up of the dimensions of the other two. The dimensions of the remaining independent variables and the dependent variable can, however, be made up of those as follows:

$$\begin{cases} [\varepsilon_k] = 1, [v] = 1 \\ [x] = [\alpha], [z] = [\alpha] \\ [t] = [P]/[E] \end{cases} \tag{29}$$

The above remaining values can get non-dimensionalized as follows:

$$\begin{cases} \Pi_0 = \varepsilon_k, \Pi_1 = v \\ \Pi_2 = \dfrac{x}{\alpha}, \Pi_3 = \dfrac{z}{\alpha} \\ \Pi_4 = \dfrac{P}{E \cdot t} \end{cases} \tag{30}$$

Applying the Buckingham's Pi-Theorem [46] the initial equation is non-dimensionalized, thus reducing the initially 7 independent variables to only 4:

$$\Pi_0 = h(\Pi_1, \Pi_2, \Pi_3, \Pi_4) \Rightarrow \varepsilon_k = h\left(\frac{x}{\alpha}, \frac{z}{\alpha}, \frac{P}{E \cdot t}, v\right) \tag{31}$$

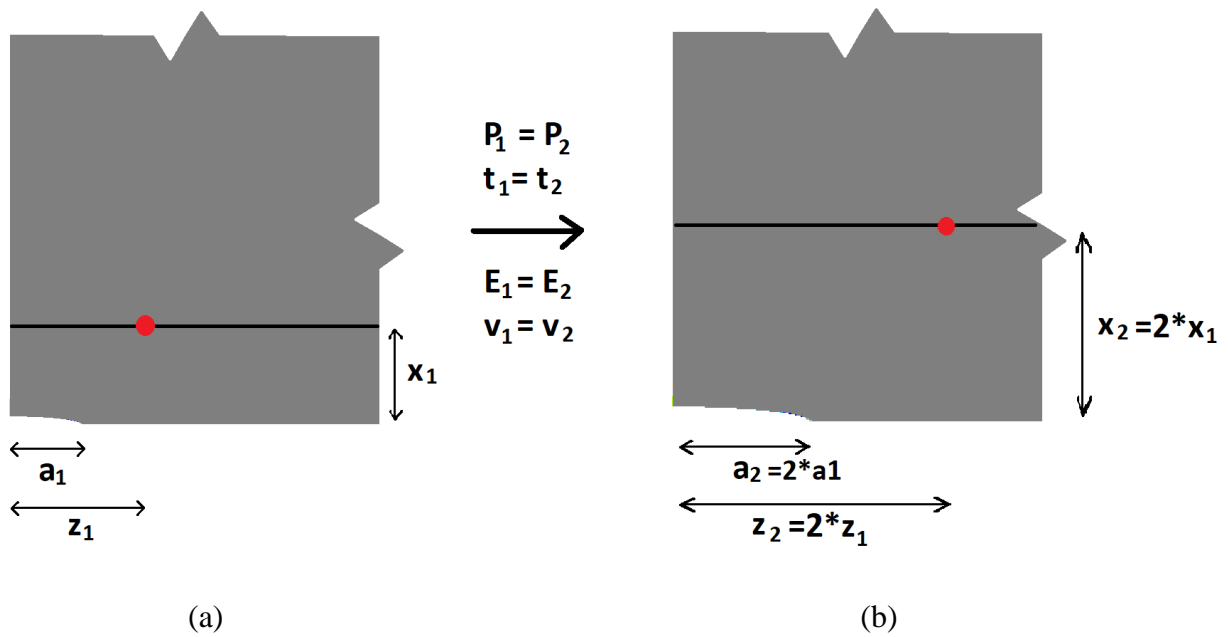Figure 35: Comparing strains from place to place using dimensional analysis

Now consider a load with a linear density of P applied to a plate of thickness t with a Young's modulus E and Poisson ratio of v as presented in Figure 35. The triaxial strain of a location (x_1, z_1) when the crack has a length of α_1 is denoted as ε_{k1}, while the triaxial strain of a location $(x_2 = 2x_1, z_2 = 2z_1)$

when the crack has a length of $\alpha_2 = 2\alpha_1$ is denoted as ε_{k2}. Geometric similarity is met due to the assumption of linear stress-strain response of the material and to the infinite width and length of the plate, so the Buckingham's Pi-Theorem can be applied for ε_{k1} and ε_{k2}:

$$\varepsilon_{k2} = h\left(\frac{x_2}{\alpha_2}, \frac{z_2}{\alpha_2}, \frac{P}{E \cdot t}, v\right) = h\left(\frac{2x_1}{2\alpha_1}, \frac{2z_1}{2\alpha_1}, \frac{P}{E \cdot t}, v\right) = \varepsilon_{k1} \tag{32}$$

An engineering intuition on the above finding is that the strain field – thus the stress – of the case depicted in Figure 35 (a) is a zoomed-out version of the Figure 35 (b). This is also visible in Figure 32-Figure 34, as the strain fields resulted by higher cracked lengths are a zoomed-in version of the ones resulted by smaller crack lengths. This is an idea that can be utilized in understanding the different sensor placement architectures following in section 4.2.3.

4.2.3. Discussion: Sensor placement

The surrogate model can be effectively utilized to construct the likelihood function of Bayesian schemes used within crack SHM. Beyond that and in order to gain a deeper intuition of the underlying physics, the surrogate model is utilized to plot the strain readings of sensors assumed to be placed at indicative locations on the plate, as depicted in Figure 32. In detail, a total of 16 candidate locations are examined, situated at the intersections of four x-directional paths ($x = 50mm, 100mm, 150mm, 200mm$) and four z-directional paths ($z = 50mm, 100mm, 200mm, 300mm$). It becomes apparent that the z-directional strain, ε_z, does not provide reliable information as the strain levels are relatively low compared to other directional strains. These low strain levels can potentially be overshadowed by the sensor's noise, which typically ranges around ±5 microstrains. In contrast x-directional strain ε_x and xz-plane shear strain ε_{xz} are ranging considerably higher than the white noise level.
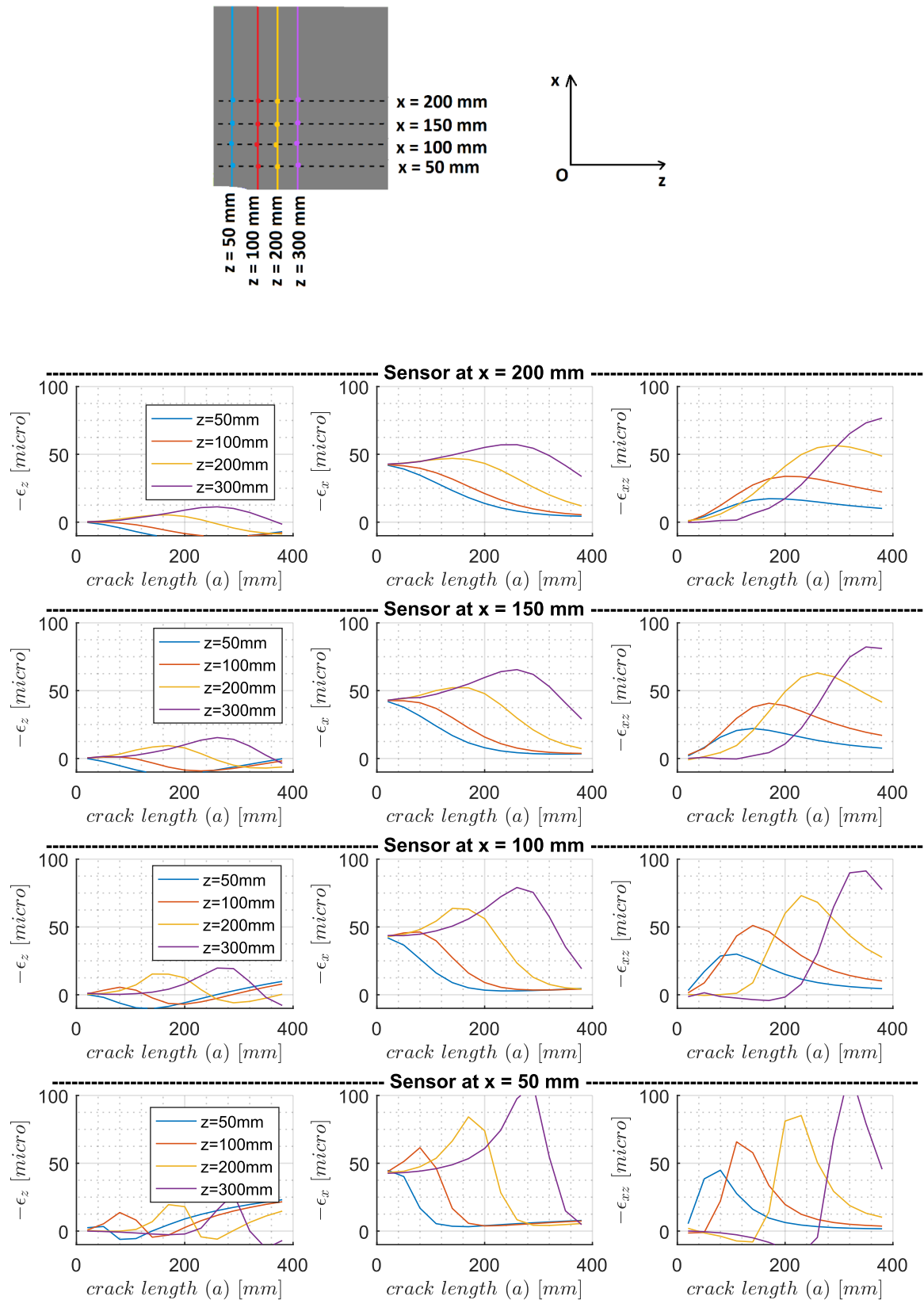
Figure 36: Sensor readings of strain sensors placed on some indicative locations
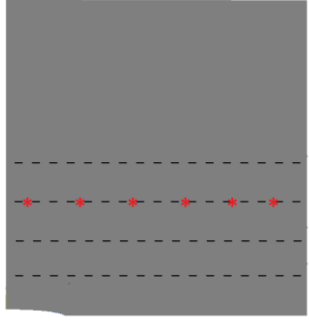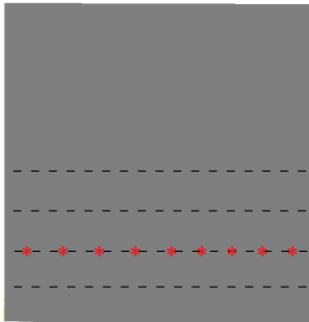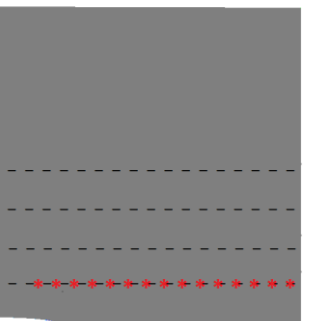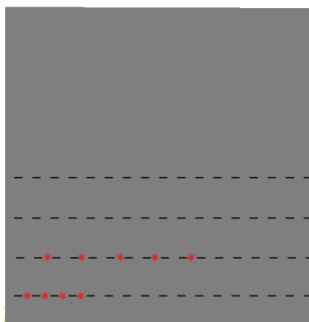
According to Section 2.5 one approach to determine an optimal sensor placement architecture is through the application of optimization theory. In this context, an optimization technique can be employed to identify the best combination of 8 available sensors among the 16 possible locations, resulting in an optimal configuration that maximizes the overall measurement performance. Mathematically, exploring all possible combinations of sensors in this case would involve studying approximately $N_C = \binom{32}{8} \simeq 10^6$ combinations. However, it is important to note that the actual problem may be even more complex, as there could be more than 16 potential sensor locations to consider. Taking into account such a large number of locations would significantly increase the computational cost and time required for the analysis. Therefore, in the present study, the sensor placement was determined using engineering judgment, as discussed in the subsequent paragraphs.

Building upon the concepts discussed in Section 2.5.2, various scenarios of sensor placement will be evaluated. First, it is evident that smaller cracks tend to be obscured by noise when measured by sensors positioned far from the crack. This phenomenon arises because, for small crack lengths, certain readings do not exhibit a one-to-one correspondence, rendering them unreliable sources of information. For instance, a sensor placed at coordinates x=200mm and z=200mm can reliably detect a minimum crack length of approximately 220mm, whereas a sensor placed at x=100mm and z=100mm can detect a minimum crack length of about 110mm, as seen in Figure 36. The observed pattern, where halving the coordinates leads to a halving of the minimum detectable crack length, is not arbitrary but can be elucidated through dimensional analysis, as expounded upon in Section 4.2.2.

Based on the aforementioned information, it becomes evident that choosing sensors closer to the crack, increases accuracy but decreases coverage. In such case, in order to monitor the total coverage of possible crack lengths (from 40mm to 400mm) a higher number of sensors have to be used as each one of them is monitoring a narrower portion of the total coverage. In contrast, choosing sensors further away from the crack, decreases accuracy but increases coverage. In such case, in order to monitor the total coverage of possible crack lengths (from 40mm to 400mm) a lower number of sensors have to be used with each monitoring a wider portion of the total coverage. So, placing sensors further away from the crack, results to reduced accuracy, but increased coverage, meaning less total number sensors. The above analysis was done for several elementary sensor placement architectures, the results of which are presented in Table 7. The total number of sensors is approximated by dividing the total coverage

demanded (400mm-40mm) with the approximate coverage per sensor for each particular architecture as derived from Figure 36 according to Section 2.5.2.

Table 7: Comparing different architectures

Archtiecture	Approximate coverage per sensor	Total no. of sensors need	Accuracy
	~100 mm	~4	Low
	~50 mm	~8	Medium
	~20 mm	~20	High
	~30 mm (x=100mm) ~20 mm (x=50mm)	~12	High

5. Conclusions

A fatigue assessment method was developed in this thesis that combines the usage of stochastic FCG models to describe the fatigue process, while spectral analysis is employed to describe the fatigue loading and presented along with all detailed mathematical procedures. The combination of those two techniques was achieved by establishing a state model where time is treated as a discretized parameter. The method, while overcoming each individual method's drawbacks, maintains their advantages, thus more accurately describing the physical phenomenon of fatigue in marine structures. While the loading uncertainty is reduced considerably, the most significant remaining uncertainty is the one related to the structure's material properties. The proposed method can be developed further in order to assess system-level fatigue in real-time while the ship is operating, without installing any equipment onboard. Moreover, the proposed method offers a robust process to generate realistic crack growth scenarios, which can be employed further for the development of SHM systems aimed at prognostics. More specifically, they can be employed within the context of preposterior analyses that may determine optimal maintenance strategies for safe lifetime extensions of cracked marine structural elements.

However even if much research power is concentrated to better determine the EIFS, it is still a variable with high uncertainty, thus making the application of the proposed method to intact plates computationally challenging. In the context of fatigue analysis in marine structures, it is common practice to model the wave spectrum encountered by a structure using a wave scatter diagram derived from a specific ocean. However, this assumption may not always accurately capture the actual loading experienced by the structure over its operational lifetime. The reason for this is that the loading experienced by a ship is dependent on its specific location in the globe over time, as well as other factors such as the vessel's heading and speed. Additionally, the sequence of encountered sea states is not fully random, since there are transient effects in play which have not been accounted for in this work. Therefore, the use of a wave scatter diagram from a particular ocean, as employed in this work, to estimate the loading on a ship can lead to either an overestimation or underestimation of the actual loading, depending on the vessel's operational profile.

In a simplified version, this method was applied in a cracked plate of a 7800 TEU VLCS, for which the RUL and PoF were estimated. For the same case study, a FEM model of the cracked structural element was created and set the basis for a surrogate model. Both these structural models and the dimensional analysis performed for the problem, contributed information that developed a physical intuition of the problem. This in turn, pointed out basic concepts on sensor placement architectures, that may support a crack SHM.

References

[1] Γ.Δ.Χρυσουλάκης, Δ.Ι.Παντελής "Επιστήμη και τεχνολογία των μεταλλικών υλικών" Παπασωτηρίου, Αθήνα 2008.

[2] Ajit Nair, K. Sivaprasad & C.G. Nandakumar | (2017) Crack assessment criteria for ship hull structure based on ship operational life, Cogent Engineering, 4:1, 1345044, DOI: 10.1080/23311916.2017.1345044.

[3] Ship Structure Committee (SSC). SSC 462: Review of current practices of fracture repair procedures for ship structures. 2012.

[4] Νικόλαος Τσούβαλης, Ναυπηγική Τεχνολογία, Πανεπιστημιακές σημειώσεις ΕΜΠ, 2018.

[5] The British Standards Institution (BS). BS 7910: Guide to methods for assessing the acceptability of flaws in metallic structures. 2015..

[6] International Association of Classification Societies. Common Structural Rules for Bulk Carriers and Oil Tankers. 2021..

[7] Proceedings of the Institution of Mechanical Engineers Part M Journal of Engineering for the Maritime Environment, July 2012, Wengang Mao, Zhiyuan li, Jonas W. Ringsberg, Igor Rychlik, Application of a ship-routing fatigue model to case studies of 2800 TEU and 4400 TEU container vessels.

[8] Dataintelo "Strain Sensor Market Research Report".

[9] Robert E. Melchers, Andre T. Beck "Structural Reliability Analysis and Prediction", Wiley 2018.

[10] Georgios I. Aravanis "Construction of Data-Driven Models for the Identification of Large-Scale Damages in Stiffened Panel GeometriesConstruction of Data-Driven Models for the Identification of Large-Scale Damages in Stiffened Panel Geometries", Diploma Thesis, 2023, DSPACE@NTUA.

[11] Hideyoshi Yanagisawa, Oto Kawamata, Kazutaka Ueda "Modeling Emotions Associated With Novelty at Variable Uncertainty Levels: A Bayesian Approach" 2019 10.3389/fncom.2019.00002.

[12] Bitner-Gregersen EM, Dong S, Fu T, Ma N, Maisondieu C, Miyake R, et al. Sea state conditions for marine structures' analysis and model tests. Ocean Engineering 2016;119:309–22. https://doi.org/https://doi.org/10.1016/j.oceaneng.2016.03.024..

[13] Γ.Α. Αθανασούλης, Δυναμική Πλοίου, Πανεπιστημιακές σημειώσεις ΕΜΠ.

[14] Goda Y. Random Seas and Design of Maritime Structures. vol. Volume 33. WORLD SCIENTIFIC; 2010. https://doi.org/doi:10.1142/7425..

[15] American Bureau of Shipping (ABS). Guide for spectral-based fatigue analysis for vessels. 2022.

[16] Luis De Gracia, Toichi Fukasawa "A Study on the Influence of Ship Weather Routing in Fatigue Life Prediction of Ship Structures" The Japan Society of Naval Architects and Ocean Engineers (JASNAOE).

[17] Wang Y. Spectral fatigue analysis of a ship structural detail – A practical case study. Int J Fatigue 2010;32:310–7. https://doi.org/10.1016/J.IJFATIGUE.2009.06.020..

[18] Mikulski Z, Lassen T. Fatigue crack initiation and subsequent crack growth in fillet welded steel joints. Int J Fatigue 2019;120:303–18. https://doi.org/10.1016/J.IJFATIGUE.2018.11.014..

[19] Giannella V. Stochastic approach to fatigue crack-growth simulation for a railway axle under input data variability. Int J Fatigue 2021;144:106044. https://doi.org/10.1016/j.ijfatigue.2020.106044..

[20] Yosri A, Leheta H, Saad-Eldeen S, Zayed A. Accumulated fatigue damage assessment of side structural details in a double hull tanker based on spectral fatigue analysis approach. Ocean Engineering 2022;251:111069. https://doi.org/10.1016/j.oceaneng.2022.111.

[21] Viswanathan A, Subramanian VA, Kumar D. Location-based fatigue damage assessment on an FPSO by the spectral analysis method. MATEC Web of Conferences 2019;272:01019. https://doi.org/10.1051/matecconf/201927201019..

[22] Kamariotis A, Sardi L, Papaioannou I, Chatzi E, Straub D. On off-line and on-line Bayesian filtering for uncertainty quantification of structural deterioration 2022..

[23] Frangopol Dan M. and Soliman M. Damage to Ship Structures Under Uncertainty: Evaluation and Prediction. In: Voyiadjis GZ, editor. Handbook of Damage Mechanics: Nano to Macro Scale for Materials and Structures, New York, NY: Springer New York; 2015, p. 565.

[24] Massel SR. Ocean Surface Waves: Their Physics and Prediction. vol. Volume 11. WORLD SCIENTIFIC; 1996. https://doi.org/doi:10.1142/2285..

[25] Li Z, Ringsberg JW, Storhaug G. Time-domain fatigue assessment of ship side-shell structures. Int J Fatigue 2013;55:276–90. https://doi.org/10.1016/j.ijfatigue.2013.07.007..

[26] Yue J, Yang K, Peng L, Guo Y. A frequency-time domain method for ship fatigue damage assessment. Ocean Engineering 2021;220:108154. https://doi.org/10.1016/J.OCEANENG.2020.108154..

[27] Lee Y, Wang Z, White N, Hirdaris SE. Time Domain Analysis of Springing and Whipping Responses Acting on a Large Container Ship. Volume 6: Ocean Engineering, ASMEDC; 2011, p. 139–47. https://doi.org/10.1115/OMAE2011-49218..

[28] Giannella V. Uncertainty quantification in fatigue crack-growth predictions. Int J Fract 2022;235:179–95. https://doi.org/10.1007/s10704-022-00624-4..

[29] Tatsis KE, Agathos K, Chatzi EN, Dertimanis VK. A hierarchical output-only Bayesian approach for online vibration-based crack detection using parametric reduced-order models. Mech Syst Signal Process 2022;167. https://doi.org/10.1016/j.ymssp.2021.108558..

[30] Silionis NE, Anyfantis KN. Static strain-based identification of extensive damages in thin-walled structures. Struct Health Monit 2022;21:2026–47. https://doi.org/10.1177/14759217211050605..

[31] Silionis NE, Anyfantis KN. Data-driven probabilistic quantification and assessment of the prediction error model in damage detection applications. Probabilistic Engineering Mechanics 2023;71. https://doi.org/10.1016/j.probengmech.2023.103412..

[32]   The British Standards Institution (BS). BS 7608: Guide to fatigue design and assessment of steel products. n.d..

[33]   Li F, Wen Z, Wu Z, Liu S, Li Z, Pei H, et al. A safe fracture fatigue life prediction based on equivalent initial flaw size. Int J Fatigue 2021;142:105957. https://doi.org/10.1016/j.ijfatigue.2020.105957..

[34]   Khalili H, Oterkus S, Barltrop N, Bharadwaj U. Updating the Distributions of Uncertain Parameters Involved in Fatigue Analysis. J Mar Sci Eng 2020;8:778. https://doi.org/10.3390/jmse8100778..

[35]   Mao W. Development of a Spectral Method and a Statistical Wave Model for Crack Propagation Prediction in Ship Structures. Journal of Ship Research 2014;58:106–16..

[36]   Qi T, Huang X, Li L. Spectral-based fatigue crack propagation prediction for very large floating structures. Marine Structures 2018;57:193–206. https://doi.org/https://doi.org/10.1016/j.marstruc.2017.10.003..

[37]   Nayak S, Panchang V. A Note on Short-term Wave Height Statistics. Aquat Procedia 2015;4:274–80. https://doi.org/10.1016/j.aqpro.2015.02.037..

[38]   Walpole R, Myers R, Myers S, Ye K. Probability & Statistics for Engineers & Scientists. 9th ed. Pearson; 2016..

[39]   Senjanović I, Malenica Š, Tomašević S. Hydroelasticity of large container ships. Marine Structures 2009;22:287–314. https://doi.org/10.1016/j.marstruc.2008.04.002..

[40]   Li M, Boulougouris E, Lazakis I, Theotokatos G. Analysis of the wave-induced vertical bending moment and comparison with the class imposed design loads for 4250 TEU container ship, 2016..

[41]   Carpinteri A, Paggi M. Are the Paris' law parameters dependent on each other? Frattura Ed Integrità Strutturale 2008;1:10–6. https://doi.org/10.3221/IGF-ESIS.02.02..

[42]   Rishi Sharma, A. Ghosh, D. Bhachawat, s. M. Ingole, A.K. Balasubramanian, U.C. Muktibodh "Assessment of Structural Integrity of Pressure Tubes during Cold Pressurization" 2014, Procedia Engineering, 10.1016/j.proeng.2014.11.049.

[43]   Hans-Jakob Schindler "Fracture Toughness of Ferritic Steels: Lower Bounds and their Implications on Testing and Application" Procedia Engineering 2014, https://doi.org/10.1016/j.proeng.2014.11.035.

[44]   Wen Zhang, Sylvie Noelle Pommier, F. Curtit, Gaëlle Leopold, Stéphan Courtin "Mode I Crack Propagation under High Cyclic Loading in 316L Stainless Steel" Procedia Materials science ELSEVIER, 2014.

[45]   Paul Judt, Andreas Ricoeur "Efficient simulation of crack growth in multiple-crack systems considering internal boundaries and interfaces" International Conference on Fracture (ICF), 2013.

[46]   Ain A. Sonin "The Physical Basis of dimensional analysis", Department of Mechanical Engineering MIT, 2001.